Spin tunnelling phenomena in single-crystal magnetic tunnel junction systems

C Tiusan, F Greullet, M Hehn, F Montaigne, S Andrieu and A Schuhl

Laboratoire de Physique des Matériaux, Nancy University, CNRS, INPL, BP 239, 54506
Vandœuvre lès Nancy Cedex, France

Abstract
A brief theoretical review points out the specific aspects of electronic
transport in single-crystal magnetic tunnel junctions employing bcc(100) Fe
electrodes and a MgO(100) insulating barrier. The theoretical predictions
are compared to the experimental reality in both equilibrium and out-of-
equilibrium regimes. For extremely small MgO thickness, we illustrate that the
equilibrium tunnel transport in Fe/MgO/Fe systems leads to antiferromagnetic
interactions. Artificial antiferromagnetic systems based on coupling by spin
polarized tunnelling have been elaborated and studied. In the out-of-equilibrium
regime and for large MgO barrier thickness, the tunnel transport validates
specific spin filtering effects in terms of symmetry of the electronic Bloch
function and symmetry-dependent wavefunction attenuation in the single-
crystal barrier. Within this framework, we explain the experimental giant tunnel
magnetoresistive effects at room temperature, up to 180%, measured in our
simple or double barrier tunnel junction systems. Moreover, we illustrate that
the magneto-transport properties of the junctions may be skilfully engineered
by adjusting the interfacial chemical and electronic structure.

(Some figures in this article are in colour only in the electronic version)

1. Introduction

The discovery in 1995 of a tunnel magnetoresistance (TMR) effect at room temperature in
amorphous aluminium oxide barrier based magnetic tunnel junctions (MTJs) [1] led to large
scale applications of MTJs in sensors and data storage devices [2].

The transport mechanisms in crystalline MTJs attracted the interest of the international
scientific community after the publication of several theoretical papers [3–5]. These showed
that a realistic description of the band structure makes the mechanisms of transport impossible
to describe within the free electron model. Indeed, in crystalline systems the Bloch electrons are
no longer more distinguished according to their orbital character but are classified with respect
to the symmetry of their associated electronic wavefunction. This determines a symmetry
dependent wavefunction attenuation within the insulator. Giant tunnel magnetoresistive

effects, reaching several thousand per cent, are theoretically predicted in single-crystal MTJs employing bcc ferromagnetic electrodes and MgO insulating barriers.

Experimental study of tunnel magnetoresistance in Fe/MgO-like crystalline systems is relatively recent. The first unfruitful developments of single-crystal MTJs were carried out in 1996 [6] and the first local spectroscopic studies reported in 2001 [7]. In 2001, Bowen *et al* obtained an encouraging magnetoresistance of 27% at room temperature [8].

Our team demonstrated experimentally that the physics of tunnelling in single-crystal Fe/MgO/Fe systems gets beyond the free-electron model [9, 10]. On the other hand, in junctions employing amorphous MgO barriers and polycrystalline electrodes, we also illustrated that the tunnelling phenomena are correctly described within the free electron framework [11]. Moreover, in single-crystal systems we illustrate the role of the interfacial electronic structure on the tunnelling [12] and recently showed that Fe/MgO interface engineering is a powerful tool for high output voltage device applications [13]. Our experimental activity within this topic has focused on a large class of MTJ systems employing MgO(100) insulating barrier and different bcc (100) electrodes such as Fe, Co, CoFe, Pd/Fe, Cr/Fe and their combination. In this paper we report TMR ratios up to 180% at room temperature in simple and double barrier MTJs with standard Fe(001) electrodes and a MgO(100) barrier. Our results are similar to those obtained by Yuasa's group (AIST, Japan) with TMR ratios in MBE grown systems below 200% [14]. The limited value of the TMR may be related to the structural quality of the epitaxial systems altered by the plastic relaxation induced by the epitaxial strains. In these circumstances a possible enhancement of the TMR ratio in epitaxial systems is still possible by increasing the polarization ratio of injected electrons. This has already been done using 'alternative' bcc ferromagnetic systems. A 410% TMR ratio has recently been reported in bcc Co/MgO/Fe MTJs by Yuasa [15]. Another way to enhance the TMR ratio requires improvement of the structural quality of the MTJ stacks. This is motivated by recent experimental results obtained in Kirschner's group [16]. They illustrate by x-ray diffraction experiments an oxygen induced symmetry and improved structural coherence in Fe/FeO/MgO/Fe(001) and Fe/FeO/MgO/FeO/Fe(001) MTJs. Moreover, in the last class of systems the theory predicts TMR ratios ten times higher than in standard Fe/MgO/Fe systems.

Interestingly, the most important values of TMR have been experimentally reported for systems elaborated by sputtering. Here the MgO barrier is mainly grown on initially amorphous electrodes subsequently re-crystallized by annealing. The plastic relaxation of the barrier is 'eliminated', i.e. the ferromagnetic electrode adopts the structure of the insulator during the annealing. In 2004, Parkin's group at IBM Almaden using an ANELVA sputtering plant reported 220% of TMR in sputtered CoFe/MgO MTJs [18] and Yuasa *et al* reported simultaneously [19] a TMR of 230%. Since these first results, the filtering efficiency reflected by the TMR ratio has been continuously enhanced. This was done by using CoFeB amorphous electrodes of different stoichiometry re-crystallized by subsequent annealing steps. It has been shown that the filtering efficiency is strongly related to the MgO barrier thickness and the annealing procedure. A recent record TMR ratio of 472% has recently been reported [24]. Other amorphous ferromagnetic materials elaborated by sputtering, such as CoFeZr, CoZrNb and CoFeSiB, and compatible with MgO(001) barriers, are currently being investigated by different groups.

Several methods are commonly used for the sputtering technique to elaborate the MgO barrier: plasma oxidation of previously sputtered Mg metallic layers [17], direct sputtering from a MgO target [18–24] or reactive oxygen sputtering from a Mg target [21]. Depending on the elaboration technique, the TMR amplitude and the resistance–area product of the junctions may vary drastically. Finally, the best magnetoresistive results have been obtained when the MgO is directly sputtered from a MgO target.

The amplitude of the TMR ratio has been enhanced gradually with better and better understanding and control of the basic transport/spin filtering physics in single-crystal MgO based MTJ. Simultaneously, new research directions have emerged.

Spin transfer switching and spin polarization experiments have been performed in magnetic tunnel junctions with MgO (150% TMR) and AlOx barriers [23, 25]. The three to four times lower switching current density ($2–3 \times 10^6$ A cm^{-2}) for MgO based MTJs is explained by the higher tunnelling spin polarization in MgO MTJs. Radio-frequency diode effects have recently been reported [26] in single-crystal Fe/MgO MTJs. A small RF current applied to a nanometre-scale MTJ generates a measurable direct-current (dc) voltage across the device when the frequency is resonant with the spin oscillations that arise from the spin-torque effect at resonance (which can be tuned by an external magnetic field). One of the last interesting effects reported in epitaxial junctions concerns the quantum oscillation of the tunnelling conductance in fully epitaxial double barrier MTJs, by Nozaki *et al* [27].

A low resistance–area product in epitaxial MTJs is required for integration of MTJs in read-heads or high-density MRAMs and in MTJ-MRAM devices where the magnetization is switched by a critical current by a spin-torque mechanism. However, when the thickness of the MgO is reduced, the filtering efficiency within the MgO is reduced. Recent results [22] report a reduction of TMR from 270 to 138% in 2.4 Ω μm^2 low resistive junctions. Despite the progress recorded made the last few years, this area remains fully opened to research.

In this paper we would like to address some fundamental aspects concerning the physics of spin and symmetry filtering in single-crystal MTJs. They concern mainly the MTJs elaborated by molecular beam epitaxy. However, one can consider that in the sputtered samples the basic hypotheses still remain valid. Indeed, if one assumes that in the sputtered samples one has single-crystal grains with well defined (100) texture and possible lateral fluctuations of orientation of axes, each grain can determine a vertical single-crystal MTJ device.

The present paper is organized as follows. A first section resumes the theoretical framework of transport in single-crystal MTJs. The next sections present the experimental results on spin polarized tunnelling in Fe/MgO/Fe MTJs elaborated by molecular beam epitaxy. The magneto-transport properties are investigated in two extreme regimes. First, for extremely small MgO thickness we show that the equilibrium tunnel transport in Fe/MgO/Fe systems leads to antiferromagnetic interactions mediated by the tunnelling of the minority spin interfacial resonance state. Secondly, for large MgO barrier thickness, the tunnel transport in simple or double tunnel junction devices validates specific spin filtering effects in terms of symmetry of the electronic Bloch function and symmetry-dependent wavefunction attenuation in the single-crystal barrier. We emphasize the crucial role of the interfaces in the tunnelling and on the spin filtering efficiency.

2. Theoretical background

2.1. Polycrystalline MTJs

In polycrystalline systems the crystallographic axes have a random distribution. Therefore, their properties are isotropic, i.e. the electronic transport is independent of the direction of propagation. The physics of transport in these systems is well described within the free-electron model. The electrons of spin σ see a constant potential in the ferromagnetic materials and are described by an effective mass m_σ. In the simplest approach the tunnel barrier is rectangular (figure 1) if the work functions of the two ferromagnetic materials are identical, or trapezoidal if they are different. The transport is described using a model with two conductivity channels, each channel being associated with one spin. Due to the exchange splitting, described in terms
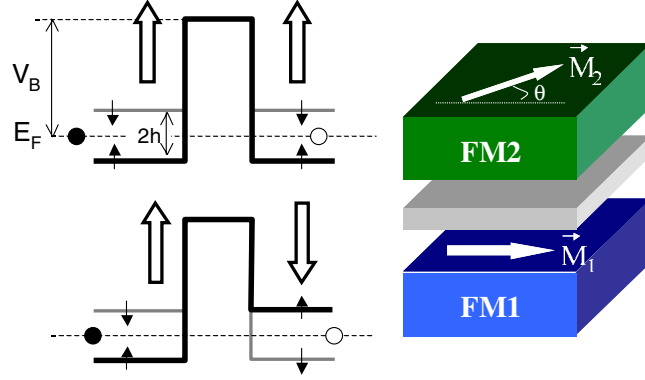
Figure 1. Left panel: potential profile seen by up (thick line) and down spins (thin line) in a magnetic tunnel junction, in the parallel (top) and anti-parallel configurations of magnetization. The exchange splitting in the ferromagnets is $2h$. The rectangular barrier height is V_B, and we denoted the energy of the electrons at the Fermi level by E_F. Right panel: schematic representation of a magnetic tunnel junction composed of two ferromagnetic layers FM1 and FM2 separated by a thin insulating barrier. The magnetization of the two FM layers can be adjusted independently; here we illustrate a configuration where the angle between $\vec{M}_1$ and $\vec{M}_2$ is θ.

of a molecular field h, the potential seen by the up and down spins in the ferromagnets is different.

In the ferromagnetic electrodes of the MTJ the electrons are described by plane waves $\Psi_i^\sigma \propto \exp(\mathrm{i}k_i^\sigma r)$, where $\sigma = \pm 1$ denotes the up ($\uparrow$) and down ($\downarrow$) spins and the $k_i^\sigma = \sqrt{\frac{2m_\sigma}{\hbar^2}(E + h\sigma)}$ is the spin dependent wavevector for an electron having energy E and an effective mass m_σ in the ferromagnetic electrodes $i = 1, 2$.

In the barrier, the wavefunction of the electrons is evanescent $\Psi_\sigma \propto \exp(-\kappa^\sigma r)$, the wavevector being given by $\kappa^\sigma = \sqrt{\frac{2m_\sigma}{\hbar^2}(V_B - E)}$, where V_B represents the barrier height. Within the free-electron model, for the large barrier thickness limit, the attenuation of the wavefunction will be $T_\sigma \propto \exp(-2\kappa^\sigma d)$, where d represents the rectangular barrier thickness. One can calculate the spin dependent transmission and the charge and spin currents for a given relative orientation θ of magnetization in the two ferromagnetic electrodes [28] of the junction. In the thick barrier limit one find that the conductivity is a linear function of the cosine angle θ between the magnetic moments of the films:

$$G(\theta) = G_0(1 + P_1^{\mathrm{eff}} P_2^{\mathrm{eff}} \cos(\theta))$$

where

$$G_0 = \frac{\kappa}{\hbar d} \left[\frac{e\kappa(\kappa^2 + k_1^\uparrow k_1^\downarrow)(k_1^\uparrow + k_1^\downarrow)}{\pi(\kappa^2 + k_1^{\uparrow 2})(\kappa^2 + k_1^{\downarrow 2})} \right] \left[\frac{e\kappa(\kappa^2 + k_2^\uparrow k_2^\downarrow)(k_2^\uparrow + k_2^\downarrow)}{\pi(\kappa^2 + k_2^{\uparrow 2})(\kappa^2 + k_2^{\downarrow 2})} \right] \exp(-2\kappa d).$$

This describes a typical spin valve effect, the tunnel magnetoresistance being defined as the relative variation of the tunnel conductance between the parallel and anti-parallel orientation of magnetizations (one can consider an equivalent definition in terms of P and AP resistance).

$$\mathrm{TMR} = (G_P - G_{AP})/G_{AP} = (R_{AP} - R_P)/R_P.$$

Here P_i^{eff} is the effective polarization of the tunnelling electrons given by:

$$P_i^{\mathrm{eff}} = P_i \frac{\kappa^2 - k_i^\uparrow k_i^\downarrow}{\kappa^2 + k_i^\uparrow k_i^\downarrow}$$

where P_i represents the ferromagnetic electrode polarization ($i = 1, 2$) related to the spin dependent density of states $n_{i\sigma}$ given by:

$$P_i = \frac{n_i^\uparrow - n_i^\downarrow}{n_i^\uparrow + n_i^\downarrow}.$$

The ferromagnetic electrode polarization can be measured by different techniques, among which we mention here superconducting tunnelling experiments [29].

The effective polarization takes into account both the polarization of the ferromagnetic electrodes and the probability of transmission of a given state through the barrier. It therefore does not represent an intrinsic property of the ferromagnets but describes the ferromagnet/tunnel barrier couple.

A model that has been widely used to describe the tunnel magnetoresistance (based on the free-electron model) is the model of Julliere [30]. This model is extremely intuitive and relates the TMR effect to the polarization. In the standard Julliere model, the considered polarization is the polarization of the ferromagnetic electrodes (defined in terms of density of states for up and down spins). Based on the Fermi golden rule, and a two-channel model associated with each spin, the main assumption is that the tunnelling probability is only a product of the density of states in the electrodes on each side of the barrier, the transmission probability being neglected. Within this simplified approach, the TMR will be given by:

$$\text{TMR} = \frac{(n_1^\uparrow n_2^\uparrow + n_1^\downarrow n_2^\downarrow) - (n_1^\uparrow n_2^\downarrow + n_1^\downarrow n_2^\uparrow)}{(n_1^\uparrow n_2^\downarrow + n_1^\downarrow n_2^\uparrow)} = \frac{2 P_1 P_2}{(1 - P_1 P_2)}.$$

For the free electrons (parabolic bands) one can write: $P_i = (k_i^\uparrow - k_i^\downarrow)/(k_i^\uparrow + k_i^\downarrow)$.

Different tunnelling experiments have illustrated that the polarization of the ferromagnetic electrode is not suitable for correctly describing the spin filtering effects in a MTJ. If one takes into account the transmission probability by tunnelling, one has to replace the ferromagnetic polarization by the effective polarization. This will lead to a generalized Julliere model where the TMR will be described in terms of effective polarization.

Even more generally, one can derive [31] a Julliere-like formula for conductance by replacing the concept of electrode polarization by an averaged interfacial transmission polarization defined by:

$$P = \frac{\langle T^\uparrow \rangle - \langle T^\downarrow \rangle}{\langle T^\uparrow \rangle + \langle T^\downarrow \rangle}$$

where the average spin dependent transmission polarization is defined as:

$$\langle T^\sigma \rangle = \sum_{k_\parallel, i} \langle T^\sigma(k_\parallel, i; 0, j) \rangle$$

the $T^\sigma(k_\parallel, i; 0, j)$ represents the diffuse transmission probability for an electron to scatter at left interface from $(k_\parallel, i)$ on the left to $(0, j)$, where $(0, j)$ is the slowest decaying state in the barrier. In this case the conductivity is given by the Landauer formula:

$$G = \frac{e^2}{h} \sum_{k_\parallel, j; k_\parallel', i} T(k_\parallel, j; k_\parallel', i)$$

where the transmission probability can be factorized as:

$$T(k_\parallel, i; k_\parallel', l) = T_L(k_\parallel, i; 0, j) T_R(0, j; k_\parallel', l) \exp(-2\kappa(0, j)d).$$

This expression is simplified if the system has a translational symmetry ($k_\parallel$ is conserved ($k_\parallel = k_\parallel'$)). The conditions of application of the Julliere model are: (i) the tunnelling barrier has

to be thick in order to have a very small wavefunction overlap and (ii) the averaged interfacial transmission polarization must been determined for the considered electrode–barrier couple. This formalism may satisfactorily describe the tunnelling across amorphous 'thick' barriers.

Within the free-electron model some other interesting features may be calculated. Indeed, from the calculation of the spin currents one can obtain the exchange coupling effects [28].

In the equilibrium case when the tunnel junction is not biased ($V = 0$), the coupling is derived from the torque produced by rotation of the magnetization from one ferromagnetic layer relative to another. This is described in terms of a spin-flip current probability calculated from the stationary wavefunctions of the free-electron Schrödinger equation. The conservative exchange coupling strength has the form:

$$J = \frac{(U - E_F)}{8\pi^2 d^2} \frac{8\kappa^3(\kappa^2 - k_\uparrow k_\downarrow)(k_\uparrow - k_\downarrow)^2(k_\uparrow + k_\downarrow)}{(\kappa^2 + k_\uparrow^2)^2(\kappa^2 + k_\downarrow^2)^2} \, e^{-2\kappa d}.$$

The sign of the coupling is given by the term $(\kappa^2 - k^\uparrow k^\downarrow)$. Then, it can be ferromagnetic ($J > 0$) or antiferromagnetic ($J < 0$).

In the presence of the voltage ($V \neq 0$), two interesting effects are also predicted within the free-electron calculation framework of Slonczewski [28]. They involve an irreversible exchange term in the coupled dynamics of the ferromagnets. For one sign of the voltage, the effect describes a Landau–Lifshitz type relaxation. For the opposite sign of voltage, it describes a pumping action which can determine the spontaneous growth of magnetic oscillations. These out-of-equilibrium effects are widely exploited nowadays for applications concerning either the magnetization dynamics/reversal by spin-torque or the study and realization of high frequency oscillators based on spin transfer.

The free-electrons formalism has been successfully used for decades to describe the magneto-transport properties in polycrystalline MTJ [32] (typically involving amorphous aluminium oxide barriers). By fitting the experimental transport characteristics with analytical free-electrons models one can extract parameters such as the barrier width and height for a given experimental system.

2.2. Single-crystal MTJs

The physics of transport becomes more complex in single-crystal systems. Here, the space is anisotropic, the electronic properties (i.e. the transport properties) being dependent on the crystallographic direction. The potential seen by an electron has the periodicity of the crystal. Consequently, the electrons are described by Bloch wavefunctions

$$\Psi_{nk_i^\sigma}(r) = u_{nk_i^\sigma}(r) \exp(ik_i^\sigma r)$$

which are plane waves modulated by a function u_{nk} having the crystal periodicity. This implies that the wavefunction will present in-plane oscillations perpendicular to the propagation direction (z), the quantity
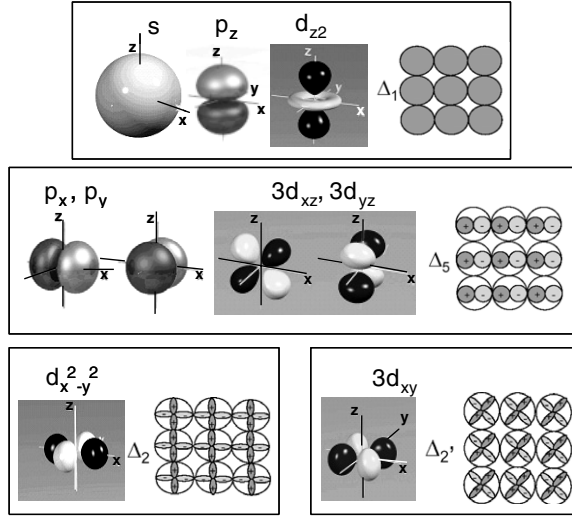
$$k_\parallel^\sigma = \frac{\langle \Psi | \frac{\partial^2}{\partial x^2} + \frac{\partial^2}{\partial y^2} | \Psi \rangle}{\langle \Psi | \Psi \rangle}$$

being nonzero.

Within the ferromagnetic electrodes the wavevector is given by

$$k_i^\sigma = \sqrt{\frac{2m_\sigma}{\hbar^2}(E + h\sigma) - k_\parallel^{\sigma 2}}$$

and in the insulator

Figure 2. The atomic-like orbital regrouped by symmetry properties. One can distinguish the orbital component of each of the symmetries Δ_1, Δ_5, Δ_2, $\Delta_{2'}$. These symmetries are particularly important for electron propagation along a direction perpendicular to the Fe(001) surface.

$$\kappa^\sigma = \sqrt{\frac{2m_\sigma}{\hbar^2}(V_B - E) + k_\parallel^{\sigma\,2}}$$

with an attenuation probability $T \sim \exp(-2\kappa^\sigma d)$. One can immediately see that the oscillations of the wavefunction parallel to the interface enhance the decay rate perpendicular to the interface ($k_\parallel \neq 0$ enhances κ). The role of the symmetry is to determine the number of nodes of the wavefunction in the plane of the interface. States that are primarily s like therefore have the smaller attenuation rate. The p-like states with more nodes are more attenuated and the d-like states typically even more so. Following this intuitive simplified picture, one can try to regroup the atomic orbitals with respect to symmetry criteria (figure 2). Within a given symmetry state, we have the same in-plane modulation. Therefore we can identify the Δ_1 symmetry regrouping (s, p_z and d_z^2) orbitals, the Δ_5 regrouping (p_x, p_y, d_{xz}, d_{yz}), Δ_2 regrouping $d_{x^2-y^2}$ and Δ_2' regrouping d_{xy}. Then we can argue that the attenuation rate of different symmetries will be different: $\kappa_{\Delta_1} < \kappa_{\Delta_5} < \kappa_{\Delta_{2,2'}}$. This simple and intuitive explanation for the symmetry dependent attenuation rate is mainly valid for vacuum barriers where, in the term $\frac{2m_\sigma}{\hbar^2}(V_B - E)$, the barrier height V_B is the same for all the symmetries. It describes correctly the attenuation in MgO barriers. However, in other oxides (i.e. SrTiO$_3$) the attenuation rate of the Δ_5 state can be lower than the one corresponding to the Δ_1. Therefore, the analysis of the complex band structure of the oxide has to be considered [33–35] in order to determine the corresponding attenuation rate for each symmetry. In the case of the MgO barrier the simple explanation remains valid. Indeed, from the complex band structure one gets that the barrier heights corresponding to the different symmetries verify the relation $V_B^{\Delta_1} < V_B^{\Delta_5} < V_B^{\Delta_2}$. This is not the case for example for SrTiO$_3$ [33–35].

This simple model is highly intuitive but is insufficient to describe some important phenomena that are predicted to occur in realistic systems. In order to correctly describe the physics of tunnelling in single-crystal systems, one has to involve *ab initio* calculations. Most frequently, these calculations are performed using the LKKR technique [3, 4]. The main results of these calculations are summarized below.
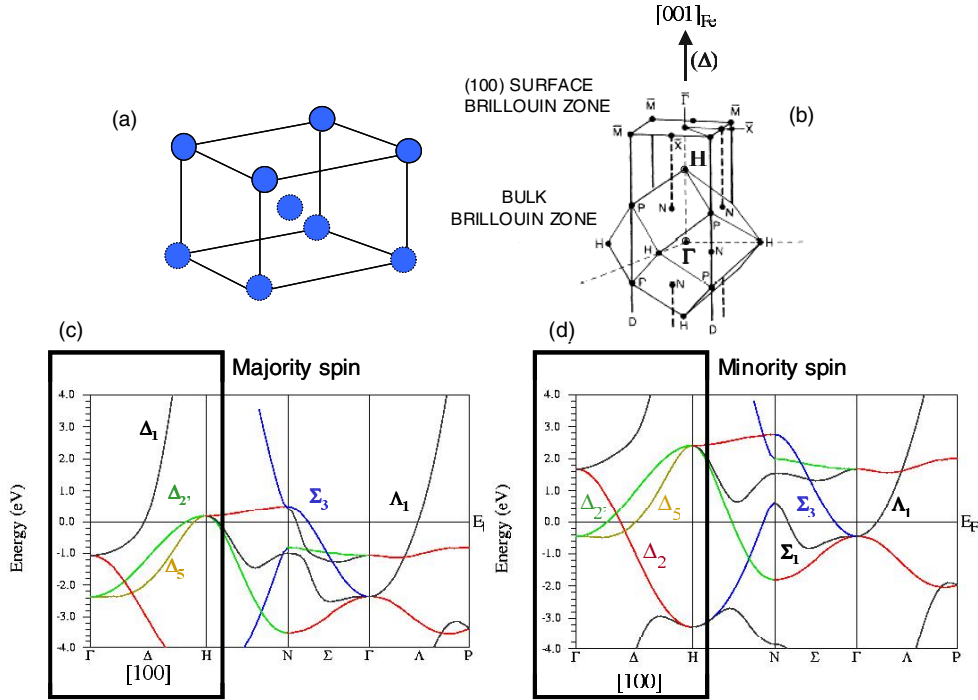
Figure 3. (a) Real space and (b) reciprocal space (right) representation of the bcc Fe lattice. For the reciprocal space (Brillouin zone) one can distinguish the high symmetry points and also the specific (Γ–H) direction denoted by Δ. This direction corresponds to the propagation of electrons perpendicular to the (100) plane in real space. The (100) surface Brillouin zone is also represented; one can distinguished the specific direction $\bar{\Gamma}$–$\bar{X}$ where the $k_{\parallel}$ is 0 in $\bar{\Gamma}$. (c) Bulk band structure diagram for the majority spin of bcc Fe. (d) Bulk band structure diagram for the minority spin of bcc Fe. We highlighted the Γ–H direction corresponding to propagating electrons perpendicular to the (100) surface of Fe ($k_{\parallel} = 0$). The states along this direction are labelled by Δ, the different indices corresponding to different symmetries of the wavefunction (see the figure for the orbital composition of each symmetry). One can see that at the Fermi level one can find spin dependent states, i.e. there is no Δ_1 state for the minority spin. This half metallic behaviour of Fe with respect to a given symmetry is only valid along the Δ direction. The other directions illustrated in the band structure diagrams are (Σ) corresponding to the (110) direction and Λ corresponding to (111) in real space.

In agreement with the intuitive explanation based on lateral variation of the wavefunction, the large TMR ratios in single-crystal tunnel junctions are determined by the different tunnelling mechanisms and symmetry-related decay rates of the Bloch waves for the majority and the minority spin channels. Roughly, an emitter single-crystalline ferromagnetic (FM) electrode filters the electrons in terms of symmetry; these are subsequently injected across the insulating (I) barrier. The filtering effect can be easily understood from figure 3 where we illustrate the bulk band structure of bcc Fe, along the high symmetry Γ–H direction, for the majority and minority spins. The direction $\Delta = \Gamma$–H corresponds to electrons with $k_{\parallel} = 0$, which propagate along the (100) direction in the crystal. At the Fermi level for the majority electrons, we have the following states: a Δ_1 (spd-like character state), a Δ_5 (pd) and a Δ_2' (d). Due to the exchange splitting, at E_{F}, there is no Δ_1 state for the minority spin. Therefore, one can immediately see that the Fe behaves as a half-metal in terms of the Δ_1 symmetry and that this is only valid for the (100) (Δ) direction. The tunnel transport probes: (i) the differences in spin injection (extraction) efficiency (directly related to the interfacial FM/I matching/coupling)
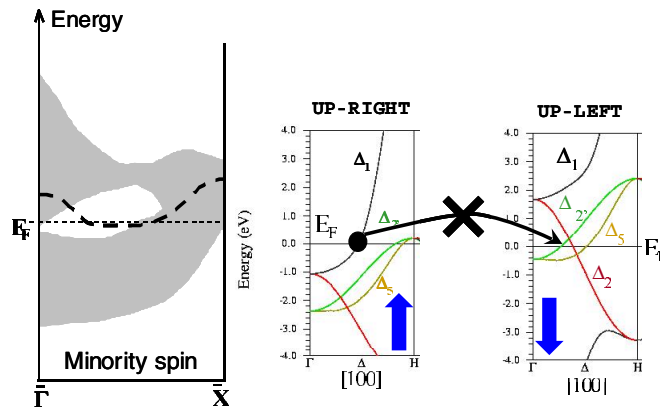
Figure 4. Left: schematic band structure diagram for the minority spin along the $\bar{\Gamma}$–$\bar{X}$ direction of the (100)Fe surface Brillouin zone. Along this direction $k_\parallel$ varies ($k_\parallel = 0$ in $\bar{\Gamma}$). The grey area corresponds to the bulk bands. The thick dashed line depicts the dispersion of the minority surface state of Fe. When this state crosses a bulk band it becomes interfacial resonance. Right: bulk band structure representation corresponding to $k_\parallel = 0$ for the majority spin channel propagation from one electrode of the MTJ to the other one when the electrodes are in the anti-parallel configuration of their magnetizations. One can see that an injected Δ_1 state from one side cannot find an equivalent symmetry state on the other side, its propagation then being forbidden. However, if one takes into account the interfacial resonance of Fe which is d_{z^2} like and belongs to the Δ_1 symmetry, an injected Δ_1 could propagate via an interfacial resonance of the opposite electrode in the anti-parallel configuration.

and (ii) the differences in decay rates when tunnelling across the barrier. The epitaxial growth of the MgO on Fe, via a rotation of the MgO lattice with respect to the Fe one by 45°, provides the symmetry conservation across the junction stack. The *ab initio* calculations [3, 5] confirm that the Δ_1 state has the smallest decay rate across the MgO, followed by the Δ_5 then the $\Delta_{2,(2')}$.

Consequently, for large MgO thickness in the asymptotic regime and in the parallel (P) configuration, the tunnelling is found to be governed by the Δ_1 state. The conductance in the anti-parallel (AP) configuration is very low, being only related to the $\Delta_{5,(2')}$ state propagation with a larger decay rate. In the AP configuration, an injected Δ_1 state cannot find equivalent symmetry in the opposite electrode with reversed magnetization. The spin asymmetry is predicted to increase above 1000%. On the contrary, when the thickness of the insulating layer decreases, the contribution of the double degenerate pd character state Δ_5 and even $\Delta_{2,(2')}$ becomes significant, the conductance in the AP state increases and therefore the TMR ratio decreases.

The above simplified picture for tunnelling summarizes the main results of the theoretical predictions [3, 5] considering only the simplified situation where we analyse the electrons having $k_\parallel = 0$. This is essentially valid for large insulating thickness (asymptotic regime). The situation gets more complex at low MgO thickness, where the contribution of $k_\parallel \neq 0$ electrons becomes significant. Moreover, in the small MgO barrier thickness regime, the tunnel transmission becomes strongly affected by resonant effects at the interfaces [3, 5, 37, 38]. Indeed, for the Fe(001)/MgO interface, an interfacial minority state is found above the Fermi energy. This is represented in the sketched diagram of the minority surface band structure of Fe(001) shown in figure 4 (left panel). The surface state crosses E_F for a specific value $k_\parallel \neq 0$. Its contribution to the conduction becomes significant when it lies within a bulk band (grey areas in the diagram), situation when the surface state becomes an interfacial resonance state (IRS). Such interfacial resonances, from both sides of the barrier,

may couple to each other, leading to a resonant tunnelling mechanism [37] which manifests itself as spikes in the conductance distribution in particular $k_{\parallel}$ points in the two-dimensional Brillouin zone. The width of these spikes is determined by the strength of the coupling in the barrier, which decreases exponentially with the barrier thickness. Consequently, the conductance from an interfacial resonance state is particularly important for extremely thin barriers. Here, the contribution of the resonant assisted tunnelling is major even in the equilibrium regime, and determines the antiferromagnetic coupling interactions observed in our Fe/MgO/Fe system [39]. Alternatively, the contribution to the tunnelling of an interfacial state may be activated by biasing the junction at finite bias voltage, even for the large MgO thickness regime. This can strongly affect the amplitude of the TMR effects.

Indeed, the large filtering effect in the Fe/MgO MTJ is related to the half metallic properties of Fe(001) with respect to the Δ_1 symmetry which can propagate only in the parallel configuration and should be blocked in the anti-parallel one. If one consider only the bulk contribution to the tunnelling, in the AP state an injected Δ_1 state should not find an equivalent state on the opposite electrode with opposite orientation of magnetization (see the diagrams in the right panel of figure 4). If one now takes into account the interface electronic structure, one can see that the surface state of Fe(001) belongs to the Δ_1 symmetry (it has d_{z^2} orbital character). This state may activate a resonant conduction channel in the AP configuration. This will drastically reduce the conductance contrast between the P and AP state and therefore the TMR. Moreover, the AP conductance associated with the interfacial resonance may become in some specific situations larger than the conductance in the parallel state. Then the TMR ratio will become negative, as shown experimentally in the paragraph dedicated to transport properties of MTJs. An important point is worth mentioning here. The signs of the bulk and the interface polarization of Fe(001) are opposite. Whereas the bulk electronic structure provides a high positive polarization (100% with respect to Δ_1 state), the interface provides a 100% negative polarization, related to the minority spin surface state. Then, the coupling of the interface to the bulk, which determines its contribution to the tunnelling, will have an extremely important impact on the amplitude of the positive TMR effects expected. Theoretically, one should neglect the contribution to the direct tunnelling of interfacial resonances expected to be strongly attenuated in the asymptotic regime. However, in real systems, diffusion mechanisms may enhance the coupling of the interface to the bulk. Then the very low conductance regime of the AP configuration can be extremely sensitive to each new channel which may be activated for conduction. Recently theoretical results obtained by the team of Tsymbal [46] have shown that the surface state of the Fe can be quenched if one intercalates a thin Ag overlayer between the Fe and the MgO, without affecting the positive polarization of the Δ_1 state.

Based on the results of the *ab initio* calculation, we can suggest a simplified model for the tunnel transport in an epitaxial MTJ. The following basic hypotheses are assumed. The main one concerns the conservation of symmetry across the stack and the conservation of $k_{\parallel}$. The transport occurs in a multichannel scheme, each channel being associated with a given spin and symmetry of wavefunction. In a perfect system we suppose that the spin and the symmetry are conserved during the transport across the MTJ stack. However, in a real system one can imagine spin-flip events or equivalent symmetry-flip events (or symmetry remixing). If the spin-flip events are related to electron–magnon interactions, the symmetry flip can be induced by diffusion events on local potential with a specific spatial symmetry. Therefore, the structural quality of the MTJ stack which will ensure the conservation of symmetry will have a strong impact on the amplitude of the filtering effects. Scattering events can also change the k (elastic) and/or the energy of the propagating wavefunction which may complicate the transport modelling. Following figure 5, one can distinguish the role of the MTJ electrodes and barrier. The ferromagnetic emitter selects the different injected symmetries,
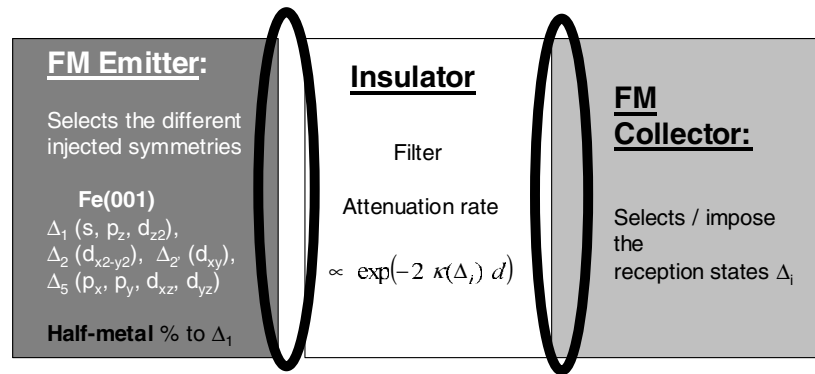
Figure 5. Simplified model of a single-crystal magnetic tunnel junction. The model assumes independent propagating channels, each channel being associated with a given spin and a given symmetry of the wavefunction. As illustrated in figure 3, the ferromagnetic emitter selects the different wavefunction symmetries which will be injected across the barrier. The collector imposes the received states. A given state will be accepted or not if an equivalent symmetry is available in the collector. The single-crystal barrier provides a special filtering effect: the attenuation rate of the wavefunction depends on its symmetry. The three subsystems are coupled by the interfaces where the wavefunction are matched. The interfaces will therefore have a major role in electron propagation.

the insulating barrier provides a symmetry dependent attenuation rate and the ferromagnetic collector selects/imposes the reception states. However, the coherent transport implicates the wavefunction matching at the interface. One can immediately understand that the interfaces will have a strong impact on the tunnel characteristics. Therefore, one can engineer the spin filtering features and the magneto-transport characteristics by controlling the interfacial electronic and chemical structure.

3. Sample elaboration

The MTJ multilayer stacks used to our studies were elaborated by molecular beam epitaxy (MBE) in a chamber with a base pressure of 5×10^{-11} mbar. The samples were grown on (100) MgO substrates, previously annealed at 600 °C for 20 min. This annealing stage does not completely remove the carbon impurities from the substrate. In order to trap the C on the substrate, a 10 nm thick seed MgO underlayer can be grown at 450 °C on the substrate before the deposition of the 50 nm thick Fe layer at 100 °C. This Fe layer represents the bottom soft magnetic layer of the junction. To improve its surface quality, the bottom Fe layer was annealed at 450 °C for 20 min. The surface RMS roughness after annealing, estimated from atomic force microscope analysis, was about 0.3 nm. However, post-annealing of the Fe top surfaces is not equivalent for samples where the diffusion of carbon was not trapped by the MgO underlayer. This is highlighted in figure 6 containing reflectance high energy electron diffraction (RHEED) patterns. For both sets of samples the RHEED patterns along the [110] direction (not shown here) are identical and they are characteristic of the cubic bcc Fe structure. However, along the [100] direction, the RHEED analysis of a sample where the C is not trapped (type A) emphasizes a 2×2 reconstruction-related additional pattern, not present for the sample where C is trapped (type B). A complete RHEED analysis concludes that in samples of type A, the Fe surface post-annealing presents a $c(2 \times 2)$ superstructure. In agreement with results of previous Auger electron spectroscopy and quantitative low-energy electron diffraction (LEED) studies [42], we associate this reconstruction with the segregation of C at the Fe(001) surface.
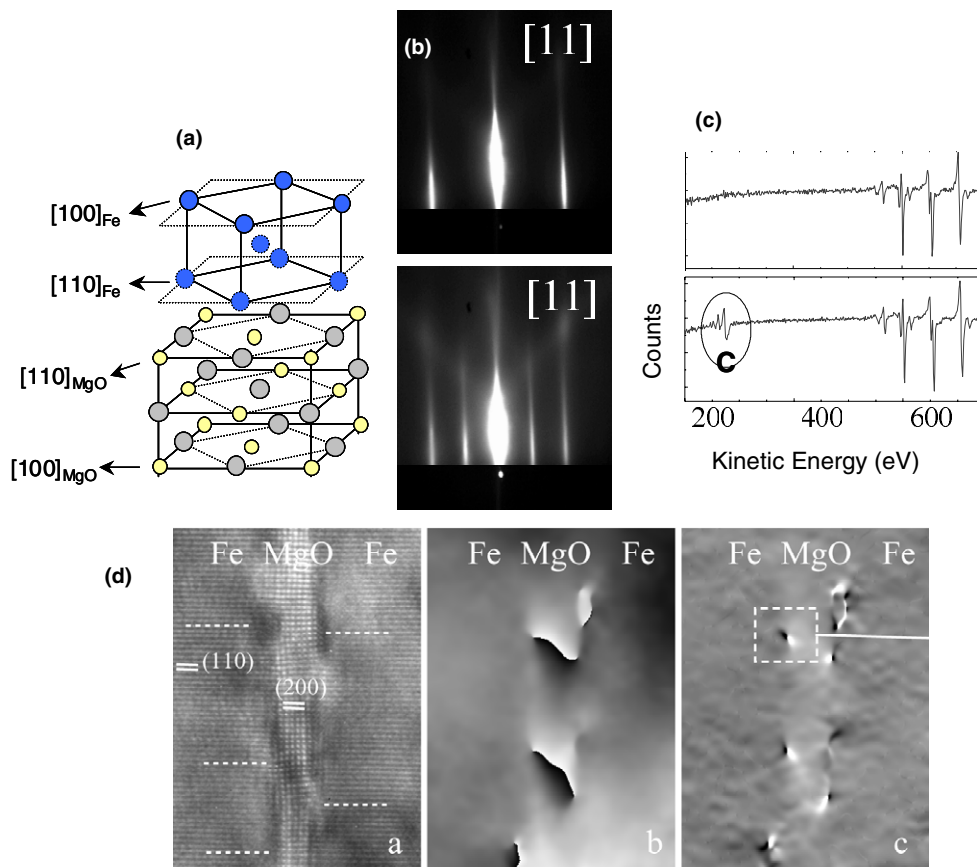
Figure 6. (a) Schematic representation of the epitaxial growth of Fe on the MgO containing the specific epitaxy relations. The Fe lattice is rotated by 45° with respect that of MgO. This lets the Δ_1 and Δ_5 symmetries be invariant. (b) RHEED patterns for the bottom Fe(100) surface along the [11] direction corresponding to a clean surface (top) and the c(2 × 2) reconstructed surface (bottom). The Auger spectra depicted in (c) validate the absence of carbon impurities for clean samples and the presence of carbon for the reconstructed surfaces. (d) Cross section high resolution transmission electron microscopy images for the Fe/MgO/Fe junctions (courtesy E Snoeck, CEMES Toulouse, France). One can remark on the epitaxial growth of the Fe/MgO system, the dark areas indicated by dashed lines indicating mismatch dislocations. The dislocations within the barrier are clearly identified in the phase image of the middle panel, whereas the dislocations at the two interfaces are clearly depicted in the phase image from the right.

The chemical nature of the surface is checked by Auger analysis. We confirmed that, for samples of type A, a carbon layer was segregated during the Fe annealing. Where does the C come from? We observed that the annealing stage of the MgO substrate at 600 °C does not desorb all the C atoms from the surface. In cases when a 10 nm thick MgO anti-diffusion underlayer is not inserted (samples of type A), the residual C atoms diffuse and segregate to the Fe top surface and provide the surface reconstruction during annealing of the bottom Fe layer. On the other hand, in type B samples, the trapping underlayer of MgO provides a C-free Fe top surface after post annealing. As will be shown in the following, the chemical structure of the Fe surface has a strong impact on the magneto-transport characteristics of the junctions, mainly reflected by the TMR versus applied voltage behaviour.

On the top of the bottom Fe layer, the MgO insulating layer is epitaxially grown by e-beam evaporation. Two-dimensional layer-by-layer growth is observed up to five monolayers by means of RHEED intensity oscillations [47]. After this critical thickness a plastic relaxation occurs inducing dislocations within the barrier. These RHEED intensity oscillations have been used to control precisely the thickness of the barrier in the extremely thin thickness range, from three to six monolayers, used for magnetic coupling studies in the equilibrium regime. For the systems used to study the magneto-transport properties out of equilibrium, the thickness of the insulating barrier ranged from 2.5 to 3.0 nm. This thickness range should correspond to the asymptotic regime, where we expect (as predicted theoretically) large magnetoresistive effects.

A second magnetic 10 nm thick Fe layer was epitaxially grown on top of the insulating MgO barrier at 100 °C. It was subsequently annealed for flattening at 380 °C for 10 min. In standard single barrier MTJ systems, this top Fe layer is magnetically hardened by a 20 nm Co overlayer. In agreement with the RHEED analysis and x-ray diffraction measurements the high resolution transmission electron spectroscopy experiments indicate a hexagonal compact packed (hcp) lattice for the cobalt layer, its six-fold axis being aligned along either the [100] or the [010] MgO direction. Therefore, two Co variants appear with the following epitaxial relation with respect to Fe: $Co(11\bar{2}0)[001] \| Fe(001)[110]$ and $Co(11\bar{2}0)[0001] \| Fe(001)[110]$.

When double barrier MTJ stacks are elaborated the top hard Co overlayer is replaced by a second thin MgO barrier and a third Fe top layer. Their structure is then as follows: $MgO \| MgO$ (10 nm)/Fe_I (50 nm)/MgO (2.5 nm)/Fe_{II} (10 nm)/MgO (0.6 nm)/Fe_{III} (20 nm)/capping. The structural quality of the Fe_{II} layer is illustrated in the RHEED patterns shown in the middle panel of figure 7. The flatness of this layer is extremely important for ensuring the continuity of a three monolayer thin MgO_{II} barrier grown on top of the Fe_{II}. The MgO thickness is precisely monitored using RHEED intensity oscillations. The top Fe_{II} (10 nm)/MgO_{II} (0.6 nm)/Fe_{III} (20 nm) subsystem behaves here as an artificial antiferromagnetic system. Its magnetic properties are driven by the exchange interactions between the two Fe layers across the barrier, as we will show in the next paragraph.

The MTJ stacks are capped with a Pd(10 nm)/Au(10 nm) protective bilayer.

The structural quality of the tunnel junction stack is illustrated by the cross-sectional transmission electron microscopy picture depicted in figure 6, using a CM30/ST microscope with a point resolution of 0.19 nm. The cross-sectional specimens were cut along (100) MgO planes. One can first see the epitaxial growth of MgO on Fe. This is a key parameter for the conservation of symmetry from the Fe electrode through the MgO barrier (conservation of $k_\|$) and has a huge impact on the Bloch wave propagation in the stack. However, dislocations located either at the bottom or at the top Fe/MgO interface (indicated in the picture by dark zones indicated by white lines and clearly seen in the phase images) induce violation of symmetry conservation and have negative effects in the symmetry filtering efficiency and may drastically reduce the TMR amplitude.

After the MBE growth, all the MTJ multilayer stacks are patterned in micrometre-sized square junctions by UV lithography and Ar ion etching, controlled step-by-step *in situ* by Auger spectroscopy.

4. Equilibrium tunnel transport—coupling regime

4.1. Non-dissipative exchange coupling

In the extremely small MgO thickness regime (three to five monolayers), in continuous films (not patterned) we observe antiferromagnetic (AF) coupling interactions at room temperature between the two ferromagnetic (F) Fe layers separated by a thin insulating tunnel barrier. We
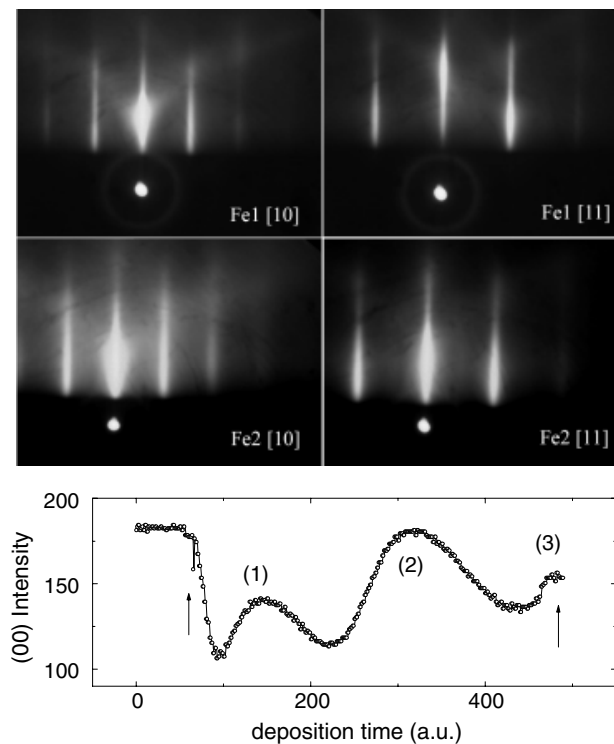
Figure 7. Top panel: RHEED patterns measured along the [10] and [11] azimuths of the square lattice of the bottom Fe$_I$. Middle panel: RHEED pattern measured along the [10] and [11] azimuths of the square lattice of the middle Fe$_{II}$. Bottom panel: RHEED oscillations observed on the (00) streak during the thin MgO barrier (of the AAF) grown at room temperature. The maxima denoted from (1) to (3) correspond to the completion of an atomic MgO layer.

associate these interactions with the transport of spin information across the insulating spacer by equilibrium quantum tunnelling of spin polarized electrons [39]. Equilibrium tunnelling implicates tunnelling of majority and minority electrons from one side of the junction to the other. In the absence of any net bias, the total current across the insulating MgO barrier is zero.

The magnetic properties have been investigated from magnetization versus field loops, performed on continuous multilayer films of standard Fe/MgO/Fe/Co systems with lateral sizes above a few millimetres, in order to avoid spurious antiferromagnetic dipolar coupling, introduced by patterning of small size devices. This analysis has already been presented in detail in our previous paper concerning interlayer coupling by spin polarized tunnelling [39]. We only report the main results here. The interlayer magnetic coupling strength J is extracted from the shift of the minor hysteresis loops (figure 8(a)), taken for the soft magnetic layer in a field window where the hard layer is magnetically 'locked' by an initial magnetization saturation. In figure 8(b), we illustrate the variation of J with the thickness t_{MgO} of the insulating barrier. We notice that AF coupling interactions have been observed in all types of junctions with and without carbon impurities at the Fe/MgO interface.

In a first step the experimental points can be adjusted by the continuous line (figure 8(b)) which represents the theoretical coupling strength computed in the simplified free-electron-like framework of Slonczewski [28]. The theoretical curve relies on effective parameters for the electronic transport, specific to the ferromagnetic Fe electrodes and the MgO insulator. Our
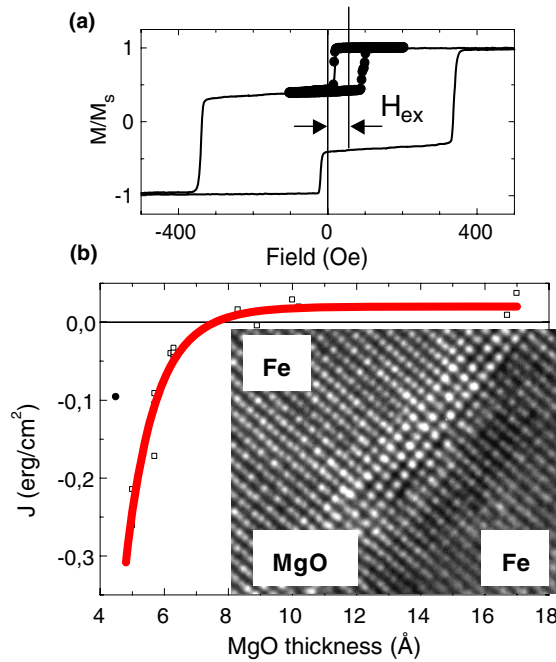
Figure 8. (a) Magnetization versus field curve for a Fe/MgO/Fe/Co system. The minor loop (-●-) represents the magnetization reversal of the bottom Fe layer, the top Fe/Co bilayer remaining locked along the positive field direction. From the positive shift of the minor loop H_{ex} we deduce the coupling strength J: $H_{ex} = J/(t_{Fe}M_S)$, where t_{Fe} is the thickness of the Fe bottom layer and M_S the saturation magnetization of Fe. (b) Variation of the coupling strength with MgO thickness. The open square points represent experimental values and the continuous line shows theoretical calculations within the Slonczewski model of coupling by spin-polarized tunnelling. Inset: cross-sectional TEM picture illustrating the pseudomorphic epitaxial growth of MgO on Fe in the low thickness regime involved in magnetic studies for coupling by tunnelling.

experimental results are in good agreement with the predictions of Slonczewski (see the section on theoretical introduction), where the equilibrium tunnelling leads to non-dissipative exchange interaction (magnetic coupling). However, the free-electron like model of Slonczewski does not take into account the specific aspects of the spin polarized tunnelling in epitaxial systems, i.e. the equilibrium propagation of different symmetry states for each spin channel, in each configuration of magnetizations: (i) in the parallel configuration the $\Delta_{1,5,2'}$ states for the majority spin and $\Delta_{5,2,2'}$ states for the minority; (ii) in the anti-parallel configuration $\Delta_{5,2'}$ state for the majority and for the minority spin.

Moreover, recently Tsymbal *et al* [40] pointed out theoretically the implication of a resonance assisted tunnelling mechanism in the AF coupling by spin polarized tunnelling. In their model, they have shown that an additional resonant tunnelling mechanism should exist in order to explain the sign of the coupling observed in our Fe/MgO/Fe junctions.

In epitaxial Fe/MgO/Fe systems, if we neglect any impurity-associated resonant levels, the interfacial minority resonance of Fe(001) provides the resonant equilibrium tunnelling mechanism, as shown in the *ab initio* calculations of Dederichs *et al* [37]. Therefore, one can assume that the equilibrium tunnel transport in the anti-parallel configuration is dominated by propagation of the interfacial resonance (related to the surface state of Fe(001)). By scanning tunnelling microscopy (STM) experiments performed on our Fe(100) samples we

clearly spectroscopically identified the Fe surface state. It has a d_{z^2} orbital character [36] belonging to the Δ_1 symmetry and is located in the minority spin channel. Moreover, our STM experiments show that the surface state of Fe is stable with respect to low-level disorder (it is not destroyed by terrace boundaries, carbon or oxygen contamination). One can imagine that some low-level disorder may even help for coupling of the surface state with the bulk bands (by elastic scattering changing the k), enhancing its contribution to the transport.

Theoretical calculations [3, 5] have shown that the interfacial resonance of Fe is preserved at the Fe(100)/MgO interface. Therefore, in a second step, we could assume that the resonant propagation of the interfacial resonance could be the main origin for the AF coupling observed in our Fe/MgO/Fe junctions. If we follow the *ab initio* analysis of tunnelling in epitaxial MTJs [3, 5], we see that the conductance related to the propagation of the interfacial resonance manifests as sharp peaks located at specific values of $k_\parallel$. The contribution to the conduction of the surface state becomes significant when it lies within a bulk band becoming an interfacial resonance state (IRS).

In the small MgO thickness regime, the carbon impurities at the Fe/MgO interface play no significant role in the tunnelling. From magnetization curve measurements describing the equilibrium (zero bias) transport properties no significant effect of C on the antiferromagnetic interactions has been observed (similar behaviour for type A and B samples). If we consider the complex tunnelling landscape in this regime, one can see that the C–Fe bonding does not affect the d_{z^2}-like resonance state of Fe, whose propagation dominates the equilibrium tunnelling currents.

The physics of the equilibrium tunnelling presented above looks complex, due to the implication for the coupling of Bloch states with different symmetry, and also of the interfacial resonance of Fe. Moreover, in the small thickness regime one has to take into account the significant contribution to the tunnelling of electrons with $k_\parallel \neq 0$. These aspects would require a multi-channel tunnelling model, each tunnelling channel being associated with a specific symmetry or resonance state. However, a 'conciliation' with the simplified mono-channel model of Slonczewski could be made if one considers that the parameters used within this model are effective, and includes the complex aspects of multi-channel tunnelling landscape, mentioned above. Alternatively, the AF coupling could be explained by a resonant tunnel transport mechanism, as shown by Tsymbal *et al*, where the resonance is provided here by the minority spin interfacial resonance of Fe(001). Of course, other resonant mechanisms can be imagined, related to imperfections of the barrier (oxygen vacancies, impurities, structural defects, etc). However, up to now the experimental spectroscopic studies performed on our samples to check the stoichiometry of the MgO barrier have not provided any evidence of oxygen vacancies or other impurities. Moreover, in the small thickness regime the growth of the barrier is pseudomorphic (layer by layer) on Fe, no dislocations being present within the insulator. Studies based on noise measurements are currently being performed on our systems to provide more insight into the resonant transport mechanisms.

4.2. Artificial antiferromagnetic systems using spin polarized tunnelling

Using AF coupling by spin polarized tunnelling we built artificial antiferromagnetic systems (AAFs). These systems, are similar to standard AAFs [43] employing ferromagnetic layers separated by metallic nonmagnetic (NM) spacers where the coupling is provided by Ruderman–Kittel–Kasuya–Yosida (RKKY) interactions. In standard AAFs the oscillations of the coupling strength with the NM spacer thickness may be explained by quantum interference effects of the propagating plane wave wavefunction in the NM spacer [41]. When an insulating spacer is involved, the non-oscillatory monotonic decay of the coupling strength with the spacer
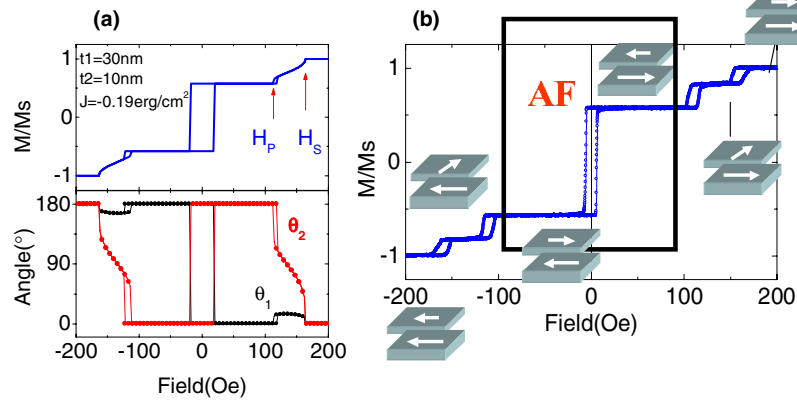
Figure 9. (a) Theoretical magnetization M–H curve along the Fe(100) easy axis calculated within a Stoner–Wolfhart macrospin model, using a numerical steepest-descent minimization procedure. The total magnetization is calculated by the equation $M(H) = (t_1 \cos(\theta_1) + t_2 \cos(\theta_2))/(t_1 + t_2)$. The field variation of the angles between the magnetization and the external field ($\theta_1(H)$ and $\theta_2(H)$) is illustrated in the bottom panel. The parameters used for the calculation are: $t_1 = 30$ nm, $t_2 = 10$ nm, $J = -0.19$ erg cm^{-2} and $K = 1 \times 10^4$ erg cm^{-3}. (b) Experimental magnetization curve corresponding to a Fe(30 nm)/MgO(0.6 nm)/Fe(10 nm), in good agreement with the theoretical simulation. We point out the magnetization configuration in the most important field windows. In the antiferromagnetic plateau, the systems behaves as a compact block of reduced magnetic moment ($M_1 - M_2$).

thickness reflects the evanescent character of the wavefunction within the barrier. The strength of the coupling, and therefore the magnetic properties of the AAF, can be experimentally adjusted by playing with the thickness of the MgO barrier. Typically, for a barrier thickness of 0.6 nm a coupling strength of -0.2 erg cm^{-2} is measured.

The magnetic properties of the AAF can be analytically explained using a Stoner–Wolfhart like model, presented in detail in the appendix. In order to simulate the magnetization versus field for an AAF one can perform the minimization of the total energy numerically (i.e. by steepest-descent, conjugated gradient or Metropolis/Monte Carlo algorithms). Such kind of simulation, for the situation when the field is applied along one of the easy axes of the bcc Fe(001), is presented in figure 9(a). If the field is higher than the saturation field H_S, the two magnetic layers of the AAF have their magnetization aligned along the field. When $H < H_S$ the magnetization of the thin layer starts to rotate, dragged by the AF coupling which tends to reverse it in the anti-parallel configuration to reduce the coupling energy. Complete reversal occurs for $H = H_P$. However, one can see during this reversal an intermediate plateau where the magnetization which reverses will remain trapped in a second anisotropy corresponding well to the second anisotropy axis for an angle $\theta_2 = \pi/2$. During the reversal of the thin layer from $\theta_2 = 0$ to π, the magnetization of the thick layer is only slightly deflected from the field direction, then in the AF plateau $\theta_1 \to 0$. The θ_i, $i = 1, 2$ represent the angles between the magnetization M_i and the field H. In the field window $-H_P < H < H_P$ the AAF behaves as a magnetically rigid monoblock with reduced magnetic moment M_1–M_2.

The theoretical simulation is in perfect agreement with the experimental results presented in figure 9(b). Here one can identify the different magnetic configurations from positive to negative saturation. The values of the plateau and the saturation field can be adjusted by playing with the thickness of the insulating barrier (which modulates the J exponentially) and with the thickness of the magnetic layers (which affects the anisotropy and the Zeeman energies).

In the last section of this paper we will see that this special kind of AAF system can be successfully used as a building block for double barrier MTJ systems. With respect to standard AAFs employing metallic polycrystalline layers [44], the AAF with epitaxial layers can have specific advantages. The anisotropy of single-crystal layers reduces the magnetic fluctuations (magnetic ripples or 360° domain wall structure). These fluctuations are responsible for parasitic magnetostatic interactions [45] and have negative effects on the magneto-transport characteristics of the MTJs. We also mention that this specific AAF which incorporates an extremely thin oxide spacer layer could be particularly interesting as a building block for spin valve metallic giant magnetoresistive devices. Indeed, the nano-oxide layer can drastically enhance the specular reflections and confine the electrons to the active part of the device and therefore enhance the magnetoresistive effect.

## 5. The out-of-equilibrium tunnel transport regime

In the asymptotic regime, at large MgO thicknesses, the symmetry dependent rate decay in the barrier reduces the number of propagating Bloch states. The filtering effect in k of the MgO barrier [3] determines a strong reduction in the conductance for electrons with $k_\parallel \neq 0$ when the thickness of MgO increases. This is assisted by the vanishing of the equilibrium tunnelling via the interfacial resonances, located at E_F for significantly large $k_\parallel \neq 0$ (figure 4). However, if we follow the left panel of figure 4, we see that the surface state of Fe may be 're-activated' by biasing the junction. Indeed, the interfacial resonance may assist the propagation of hot electrons with $E = E_F + eV$ around $k_\parallel = 0$. From the surface band diagram depicted in figure 4 one can see that above E_F the surface state disperses toward $\bar{\Gamma}$ and at $k_\parallel = 0$ it behaves as an interfacial resonance. Its coupling to the bulk allows a significant contribution to the conductance.

However, it is important to mention that for large thicknesses the structural quality of the MgO layer is slightly reduced. Indeed, after a pseudomorphic growth of MgO on Fe up to about five monolayers, the strains induce a plastic relaxation (see figure 6(d)). This will determine dislocations within the barrier. Moreover, we also have to mention the misfit dislocations at the bottom and top Fe/MgO interfaces due to the relaxation of thick Fe layers (electrodes) grown on MgO. All these local 'defects' determine a local symmetry breaking (the conservation of $k_\parallel$ is locally destroyed). Therefore, they are responsible for scattering events with negative re-mixing effects on the symmetry filtering. One can associate with each local defect a 'parasitic' conduction channel. This experimental reality separates the real transport mechanisms from the theoretical analytical framework valid for perfect single-crystalline stacks where the $k_\parallel$ is fully conserved.

The analysis of the large MgO thickness regime is performed using magneto-transport measurements (non-equilibrium transport) on patterned tunnel junctions, with lateral sizes between 10 and 200 μm.

### 5.1. MTJs with clean Fe/MgO interfaces

Lets us first consider the TMR(V) characteristics illustrated in figure 10, measured on a sample with a C free Fe/MgO interface. In agreement with theoretical predictions [3, 5], the TMR ratio is large (around 180% at room temperature), as illustrated by figure 10(a). For the thickness range of the barrier (here 2.5 nm), the tunnelling is expected to be dominated by the propagation of Δ_1 (and Δ_5) in the parallel (P) configuration and only by Δ_5 in the anti-parallel (AP) configuration. The other symmetries should be completely attenuated in this thickness regime.
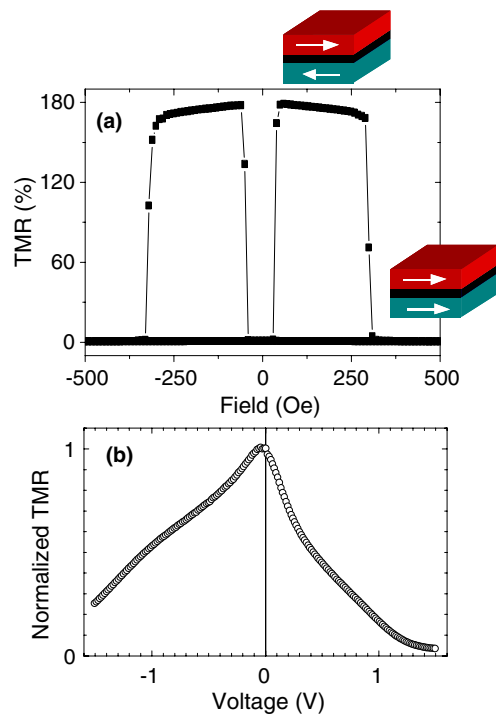
Figure 10. (a) Typical tunnel magnetoresistance curve for a Fe(40 nm)/MgO(2.5 nm)/ Fe(10 nm)/Co(20 nm) MTJ measured for a 20 μm square junction. The area–resistance of the junctions for this MgO thickness is within the 10^6 Ω μm^2 range. One can identify the two states of resistance corresponding to the parallel and anti-parallel magnetization configurations. (b) Variation of the magnetization with respect to the bias voltage. In positive bias, the current flows from the top to the bottom electrode of the MTJ. The curve looks slightly asymmetric in positive and negative voltage.

Furthermore, the TMR ratio varies significantly with the voltage (figure 10(b)), especially in the low voltage range. The slightly asymmetric bias dependence can be explained by the asymmetric top and bottom Fe/MgO interfaces in terms of roughness, structural defects (dislocations) and lattice distortions (the electronic structure of the top and bottom interfacial Fe may be slightly different due to differences in the lattice parameter). The limited maximum value of the TMR with respect to theoretical predictions implicates a reduction of the filtering efficiency, possibly due to structural imperfections and parasitic conductance channels enumerated above, over our large area junctions.

In order to get more details on the conductance channels which contribute to the transport we analyse the experimental conductance illustrated in the top panel of figure 11(a), associated with the parallel and anti-parallel magnetization configurations. In all the figures presented below the conductance is defined as $G = I/V$. From the conductance in the P configuration (see the zoom of figure 11(a)) one identify at low voltage the contribution of two conductance channels: Δ_1 and Δ_5. Indeed, from the band diagram depicted in figure 11(b) one can see that the top of the Δ_5 band lies at about 0.2 eV above E_F. This means that at low voltages (below 0.2 V) this state may contribute to the transport. An injected Δ_5 state from the E_F of the right electrode finds an equivalent unoccupied state on the other side. The conductance of the Δ_5 channel is added to the conductance of the Δ_1, as is schematically represented in figure 11(b). Indeed, at low voltage the contribution of Δ_5 enhances the parabolic conductance associated
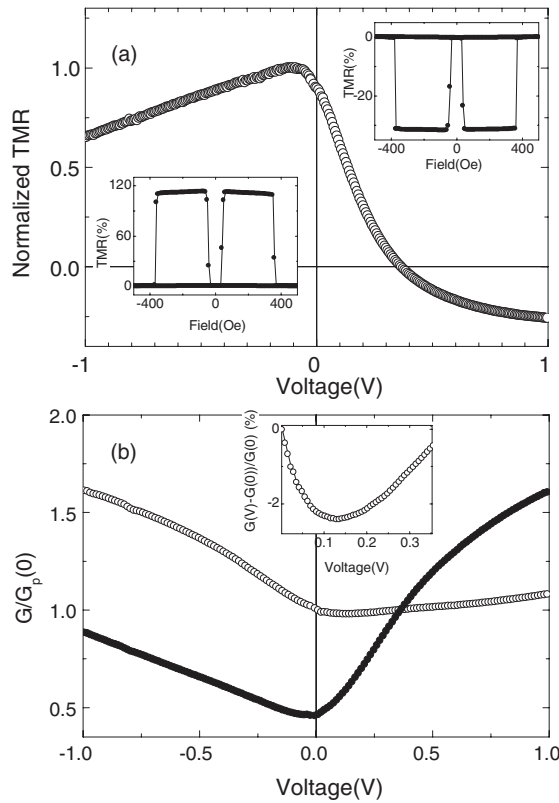
19
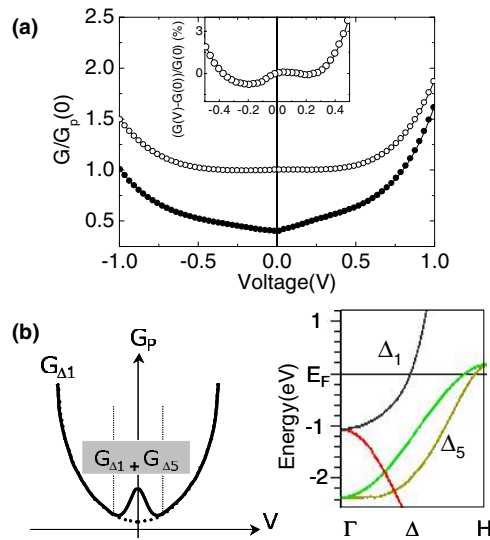
Figure 11. (a) Conductance versus voltage curve, in the parallel (-○-), respectively anti-parallel (-●-), configuration of magnetization. Zoom: relative variation of parallel conductance in the small positive voltage regime, around the two local minima. (b) Schematic model used to explain the two local minima. Based on the multi-channel model of tunnelling, they result from the superposition of a parabolic $G(V)$ associated with the Δ_1 state conductance channel and the Δ_5 channel available only at voltages <0.2 eV, as clearly understood from the zoom on the majority spin band structure diagram of bulk bcc Fe. From the band diagram one can observe the top of the Δ_5 band lying at 0.2 eV above the Fermi level.

with the Δ_1 state. This will lead to a total conductance which presents two minima, around 0.2 V. The contribution of the Δ_5 state in the parallel configuration implicates a reduction of the TMR. Indeed, in the AP configuration, where the propagation of the Δ_1 state is forbidden, the ratio of filtering of the Δ_5 state will determine the amplitude of the AP conductance and therefore the conductance contrast between the P and the AP configuration. Before we get deeper into the conductance mechanisms in the AP configuration we would like to analyse tunnelling transport in MTJ systems where the bottom Fe/MgO interface is chemically modified. We will show that the chemical bonding at the interface in tunnel junctions plays a crucial role in the selection of tunnelling electrons [48].

5.2. MTJs with a carbon contaminated bottom interface

We recall that by the growth technique we can control the presence of C impurities at the bottom Fe/MgO interface of Fe/MgO/Fe MTJs (as illustrated by the RHEED images from figure 6(b)). The TMR versus voltage characteristic measured on these samples appears strongly asymmetric (see the figure 12(a)) with a maximum TMR of 126% at room temperature. We explain this strong asymmetry by the enhancement of the contribution to the tunnelling of the interfacial resonance of Fe [12, 38]. However, the interfacial carbon and the c(2 × 2) reconstruction should make a significant contribution to this enhancement. Normally, as seen in clean samples (figure 11), the conductance in the AP configuration is always smaller than the parallel one, mainly related to the Δ_1 conduction channel.

Theoretical studies are in progress to explain the effect of the interfacial carbon. However, few preliminary ideas can already be advanced. The bonding between C and Fe (mainly via

Figure 12. (a) Asymmetric magneto-transport TMR versus voltage for a sample with carbon at the bottom Fe/MgO interface. In positive bias, the current flows from the top to the bottom electrode of the MTJ. Bottom inset: typical positive TMR–H loop measured at −10 mV. Top inset: negative TMR–H curve measured at +0.6 V, after the TMR sign reversal. (b) Conductance versus voltage curve, in the parallel (-○-), respectively anti-parallel (-●-), configuration of magnetization. Zoom: relative variation of parallel conductance in the small positive voltage regime, around the local minima.

s- and p-like orbitals) affects mainly the propagation of the Δ_1 symmetry, without affecting the interfacial resonance of Fe, located in a d_{z^2}-like orbital. Preliminary *ab initio* calculations [49][1] of Fe–C/MgO electronic structure show that the main effect of C on the surface state of Fe is a slight shift upwards in energy, with respect to the carbon free interface. Similar effects, concerning the localization of Δ_1 electrons in the interfacial bonding, have been reported by Butler *et al* for oxygen impurities located at the Fe/MgO interface [51]. Moreover, as long as the associated conductance of the sp-like character state Δ_1 channel is reduced, one can expect an enhancement of the relative contribution to the tunnelling of the d-like states of the bcc Fe(001) (within $\Delta_{1,5}$ symmetries). Therefore, the TMR(V) will be more sensitive to the spectroscopy of the density of d-like states of the bcc Fe(001). Moreover, one can also imagine that the periodical perturbation of the potential at the interface may determine scattering events (change in *k*), enhancing the contribution to the transport of the Fe minority

---

[1] We calculated the electronic structure of the Fe/Fe–C/MgO/Fe stack using the full potential-linear augmented plane wave (FP-LAPW) Wien2k code [50]. In our calculation, we used a supercell consisting of 10 Fe layers, sandwiched in between six MgO layers. In order to describe the Fe–C/MgO interface a monolayer of C has been alternatively considered at 0.4 Å above the interfacial Fe.
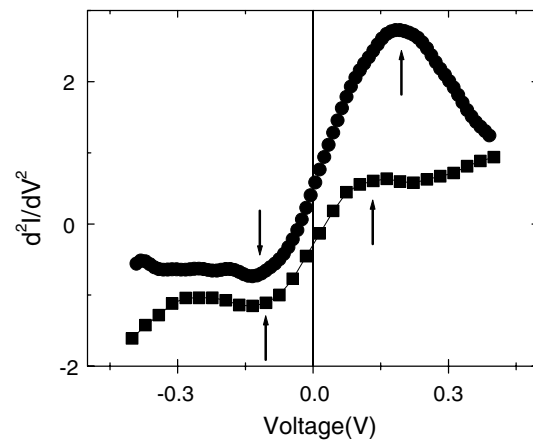
Figure 13. Second derivative of the current with respect to the voltage measured in the anti-parallel configuration of magnetization for MTJs with clean interfaces (black filled square) and a carbon contaminated bottom Fe/MgO interface (-●-). The arrows indicate the local peaks in the second derivative.

interfacial resonance. This would lead to an increase of the conductance in the AP configuration which can even overcome the P conductance. This is reflected by the negative TMR ratio measured above a few hundred millivolts in positive voltage. Indeed, in positive voltage the electrons extracted from the top Fe(001) electrode tunnel across the barrier and 'scan' in energy the bottom 'flat' Fe(001) electronic structure. When the IRS is activated a strong enhancement of the anti-parallel conductance with respect to the parallel one occurs, via the enhancement of the wavefunction matching at the interface. This is directly reflected by the sign reversal of the TMR (figure 12(a)) and by the anti-parallel conductance which overcomes the parallel one (figure 12(b)).

Here again, the P conductance presents a minimum when the energy of the hot electrons overcomes that of the Δ_5 band. The inset of figure 12(b) illustrates a variation of the P conductance of more than 2% between zero and the local minimum. Compared with the variation observed in samples with clean interfaces, one can observe that here the contribution of the Δ_5 electrons to the tunnelling is more important. The reduction of the Δ_1 related conductance by interfacial bonding between C and Fe also explains the reduction of the TMR ratio with respect to samples with clean interfaces (from 180 to below 130%).

5.3. Transport mechanisms

Tunnel spectroscopy analysis for both types of junction with clean or carbon contaminated interfaces illustrates common features in the anti-parallel configuration. Indeed, from figure 13 one can see that peaks in the second derivative of the current occur in both positive and negative voltage for both types of sample. These features determine the strong variation of the TMR with bias at low voltage. However, for samples with carbon the peak in positive voltage is significantly enhanced. This reflects the reversal of the TMR sign in positive voltage and the fact that G_{AP} becomes larger than G_P.

Several mechanism may explain the voltage variation of the TMR. These mechanisms are: (i) incoherent tunnelling due to scattering at impurities or defects located in the barrier [52]; (ii) quenching of TMR by hot electrons or spin excitation of magnons [54]; (iii) energy dependence of spin polarized DOS which affects the spin polarization [53]; (iv) intrinsic decrease related to the voltage variation of the barrier shape. In our single-crystalline MTJ, the
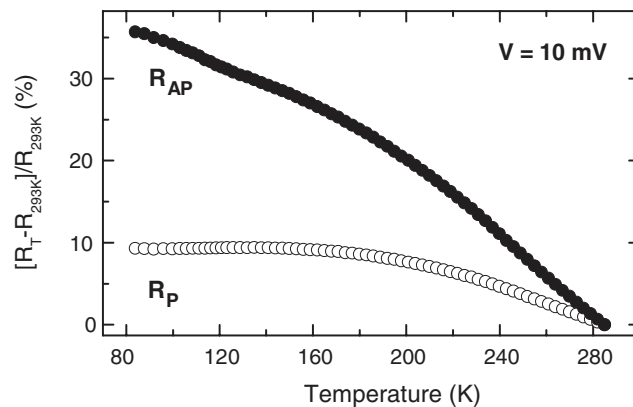
Figure 14. Typical relative variation of the junction resistance with the temperature, in the parallel (-○-) and the anti-parallel (-●-) configuration of magnetization.

first mechanism should be less important than in standard MTJs with polycrystalline electrodes and amorphous barriers. In single-crystal junctions, the quality of the insulation is rigorously controlled by the 2D epitaxial growth. However, the dislocations within the insulating barrier and at the interfaces will induce imperfect filtering effects and will complicate the analysis of tunnelling in terms of symmetry/orbital character related channels. Concerning the second mechanism, the analysis of the magnon spectra for the bcc Fe [55] and phonon spectra for MgO [56] shows no relevant peak in the magnon/phonon DOS, in the energy range where we analyse the voltage variation of the TMR. Therefore, we relate the observed TMR(V) in our junctions to the third mechanism, which points out the signature of the electronic structure in the tunnel transport characteristics. This signature is different for samples with clean or carbon contaminated interfaces which, despite a similar bottom Fe electrode, have different bottom interfaces. If we take into account the IRS located in the minority band, with a d_{z^2} orbital character belonging to the Δ_1 symmetry, one can expect a resonant tunnelling event when this IRS becomes activated. This would explain an enhancement of the AP conductance via a resonant assisted mechanism, directly related to the interfacial resonance of the Fe(001). The contribution of the IRS to the tunnelling is strongly enhanced by the presence of carbon at the bottom interface which drives the conductance to become more sensitive to d-like electrons to whose orbital character the IRS belongs.

In our explanation for the 'zero bias anomaly' observed in epitaxial Fe/MgO/Fe junctions, we excluded the implication of magnons. This was done on the basis of theoretical calculations for magnon spectra, which show no peak in the magnon DOS in the relevant energy range. However, a complete proof for the origin of the zero-bias anomaly in the dominant interfacial electronic structure should be provided by further experiments concerning transport properties at low temperature, below the freezing temperature of magnons in Fe. Moreover, our experimental results motivate further theoretical investigations which should confirm or invalidate the resonant transport mechanisms we propose here.

Studies are in progress concerning the possible influence of the interfacial carbon on symmetry remixing effects (the cubic symmetry is locally broken at the interface) or symmetry change by diffusion on localized potential perturbation associated with the periodical interfacial superstructure. These could have significant effects on the conductance channels available for the transport.

Another interesting insight is provided by analysis of the variation of the resistance with the temperature in the parallel and anti-parallel configurations. This is illustrated in figure 14.

One can see that this variation is almost four times larger in the AP configuration then in the P one. This can be easily understood if one remember that in the AP configuration, for large MgO barrier thickness, we expect a very low conductance regime. For perfect filtering, the conductance should be ideally almost zero; in our samples we showed that the AP conductance contains at least the Δ_5 state contribution.

Then, all the mechanisms which could provide additional transport channels when the temperature increases will have a major impact on the total conductance. We mention here few of them: the spin-flip events which could allow the propagation of the Δ_1 state, the elastic/inelastic diffusion on phonons or local potential perturbations which may change the k and/or the energy and open a conduction channel forbidden at $k_{\parallel} = 0$. Moreover, the direct dependence of the conductance on the electronic structure features in single-crystal MTJs may implicate strong variations with temperature if sharp features appear in the DOS within the kT window (this is the case for the minority spin for which the surface state provides a sharp peak above the E_{F}).

In the P configuration, the conductance is large, being dominated by the propagation of the Δ_1 channel which overwhelms any thermally activated conduction channels. This explain the smaller variation with temperature of the P conductance measured in our samples.

5.4. Statistical aspects concerning the spin polarized tunnelling in epitaxial MTJs

In a real junctions one can imagine fluctuations of the properties of the MTJ which will give rise to a specific statistical distribution of the tunnel currents over the surface of the junction. One of the most frequent fluctuations, already studied theoretically [57] and experimentally, is the roughness related fluctuation in the barrier width or fluctuation related to the barrier height [58]. If one assumes a Gaussian distribution of the barrier width (height), the statistical distribution of the tunnel currents will be log-normal: the broader the Gaussian distribution, the broader the log-normal distribution of tunnel currents will be. Interesting scaling effects can occur [57] when the size of the junction is varied. From an applications point of view, if one wants to reduce the size dependence of the MTJ magneto-transport properties, one has to approach as close as possible a narrow Gaussian distribution for the tunnel currents. Experimentally, using conductive atomic force microscopy experiments one can measure directly the tunnel barrier maps and extract the statistical distribution of the tunnel currents. The main purpose is to find the experimental conditions for manufacture of tunnel barriers (use homogeneous oxides, eliminate current hot-spots) which reduce the width of the current distribution [58].

If we now transpose these concepts to single-crystal systems, the situation gets more complex. First, we can eliminate the large fluctuations of thickness, having in mind epitaxial control of the growth. However, even if one gets atomic layer roughness, the filtering effect in terms of symmetry will be extremely sensitive to any local defect related to symmetry breaking. We could mention here such types of defects: terraces, misfit dislocations at interfaces and in the MgO barrier. Each defect will lead to a local higher conductance conduction channel being equivalent to a hot-spot in the classical approach. One also has to consider the fluctuation of the local electronic structure related to the specific local defect, having in mind the extreme sensitivity of magneto-transport to the electronic structure in the epitaxial MTJ.

Concerning the scaling, with respect to the micrometric size of our junctions, the effect of this kind of defect will be different. The period of dislocations is around 1 nm, therefore one considers that their effect is well averaged statistically and we have a good Gaussian distribution for junctions of micrometric size. This will provide a good scaling of the MTJ transport properties with respect to the size of the MTJ. The situation is completely different concerning the terraces, whose size is several hundred nanometres. The statistical average

effects over micrometric size surfaces is less Gaussian-like, and then one might expect large fluctuations of MTJ properties when the size of the junction varies.

The effect of the fluctuations is particularly important when one measure a low conductance state, i.e. the anti-parallel configuration of a Fe/MgO/Fe MTJ. Here, each higher conductance channel associated with a defect will raise the low conductance having an electrical shunt effect. In the parallel state, the current is dominated by a low conductance channel, increases in conductance related to local fluctuations being insignificant. Then we can deduce an interesting feature of the epitaxial MTJs: a statistical analysis of the distribution of magneto-transport properties in the parallel and anti-parallel configuration of the MTJ should be significantly different.

At the end of this section, we can compare the epitaxially grown single-crystal MTJs with similar systems grown by sputtering. Certainly, the statistical distribution of the local defects (grain boundaries) in the sputtered samples will be different from that of terraces in the epitaxial MTJs. Then, one can expect better average effects in sputter samples and better scaling of transport properties with the junction surface. However, an important source of magnetization fluctuations related to fluctuations of anisotropy is negligible in epitaxial samples with well defined magneto-crystalline anisotropy. The magnetization fluctuations can be more important in the sputtered textured samples. Here, in the AP low resistive state one can get fluctuations of magnetization in the sample related to local fluctuations of anisotropy from one magnetic grain to another. This may lead to mixed magnetic states (i.e. residual domain wall structure). A state which cannot propagate in a pure anti-parallel magnetic state could then propagate via a channel associated with another available magnetic configuration (i.e. the core of a 360° wall will provide a local parallel magnetization high conductance channel with respect to adjacent anti-parallel domains). Even if the magnetization fluctuations can be reduced by exchange anisotropy (when the exchange bias is used to pin the magnetization in sputtered MTJ samples), one still has also to consider another possible source of fluctuation which is related to fluctuation of the local crystalline quality.

5.5. Fe/MgO interface engineering for high-output-voltage device applications

For device applications, the key parameter is the magnitude of the output signal modulation, namely the output voltage defined as $V_{out} = V(R_{AP} - R_P)/R_{AP}$, where V is the applied voltage.

From the TMR ratio as a function of the bias voltage (figure 15(a)), the output voltage for device applications is plotted against the bias voltage in figure 15(b) for Fe/MgO/Fe MTJs with clean or carbon contaminated interfaces. For clean samples which provide the highest TMR amplitude, the V_{out} in positive bias voltages can exceed 300 mV. This value is already almost two times larger than the values measured for conventional MTJs with AlO barriers. However, as shown in figure 15, we illustrate here that this V_{out} can be further increased (up to almost 1 V) by interface engineering, namely the insertion of C at the Fe/MgO interface. The conventional use of high values for both TMR and $V_{1/2}$ to provide large V_{out} is replaced here by a new mechanism. The specific filtering effect related to a C contaminated Fe/MgO interfacial electronic structure induces a change of the sign of the TMR. The inverse TMR remains quasi constant at bias voltages beyond 1 V, reaching values above -40%. This, combined with the small tunnel resistance of the junction biased beyond 1 V, leads to large values of the junction output voltage and interesting features with regard to integration of MTJ sensors or data storage in devices where low resistance is required. These results illustrate how interface engineering in Fe/MgO/Fe MTJs may be used as a key technology in engineering the properties of novel spintronic devices.
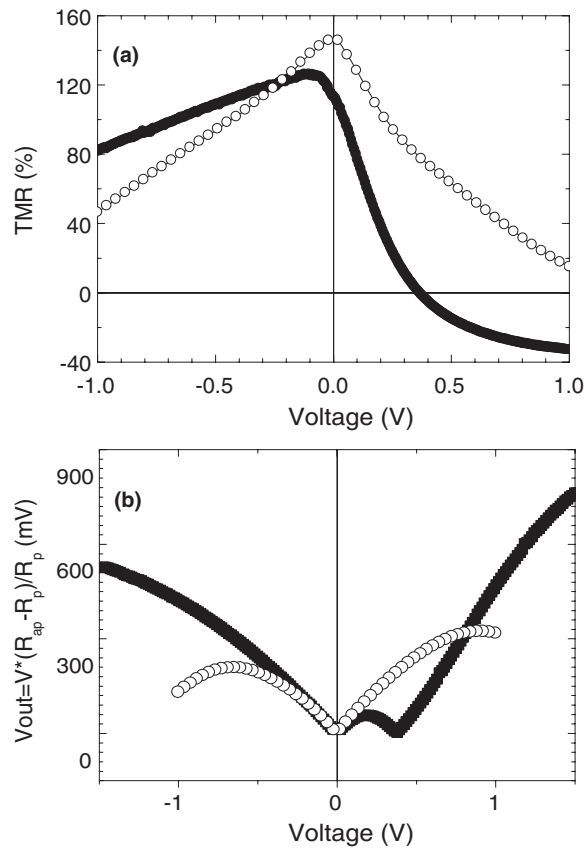
Figure 15. (a) Magnetoresistance as a function of applied voltage measured on a Fe/MgO/Fe tunnel junction (-○-) and on a Fe/C/MgO/Fe tunnel junction (-●-). (b) Output voltage versus applied voltage measured on a Fe/MgO/Fe tunnel junction (-○-) and on a Fe/C/MgO/Fe tunnel junction (-●-). In positive bias, the current flows from the top to the bottom electrode of the MTJ.

5.6. Double barrier MTJ devices involving AAF subsystems

Beyond the standard Fe/MgO/Fe MTJs, we also fabricated a new interesting class of double barrier epitaxial junctions. In these junctions, one electrode is a bottom $Fe_I(100)(45 \text{ nm})$ single-crystalline layer. It is separated by a 2.5 nm thick MgO_I layer by the other electrode, constituted by the $Fe_{II}(10 \text{ nm})/MgO_{II}(0.7 \text{ nm})/Fe_{III}(20 \text{ nm})$ artificial antiferromagnetic (AAF) system. 'Standard' AAFs, using RKKY interactions across a metallic nonmagnetic spacer, are commonly used in MTJ based devices such as read-heads or nonvolatile magnetic memories (MRAM) due to their advantages for device magnetic properties [44]. Epitaxial Fe/MgO MTJ stacks using standard RKKY based AAF type Fe/Cr/Fe have been studied by Przybylski *et al* [59]. However, the particularity of the AAFs involved in our MTJs is that the coupling is achieved across the thin MgO spacer (about three monolayers) by quantum tunnelling of electrons. The epitaxial growth of all the layers ensures conservation of the crystalline symmetry across the whole stack and provides symmetry related spin filtering effects.

Let us first consider the magnetic properties of the MTJ stack. The magnetization curve, measured on a continuous film sample prior to lithography, is presented in the top panel of figure 16. The field is applied along one of the easy axes of Fe which presents a four-fold
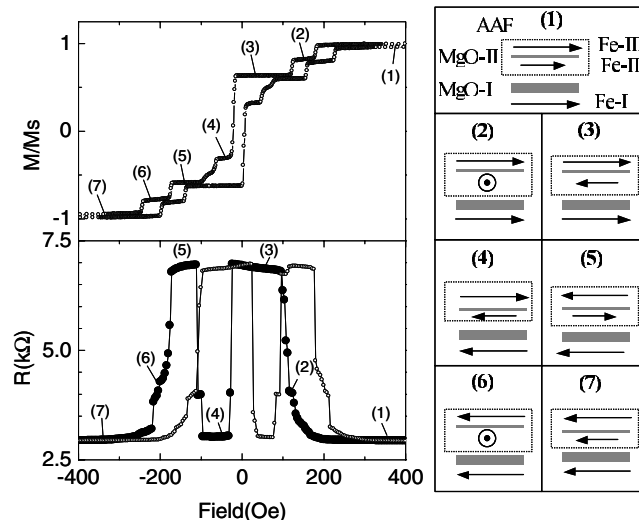
Figure 16. Top left panel: magnetization curve measured on a continuous Fe(45 nm)/MgO(2.5 nm)/Fe(10 nm)/MgO(0.7 nm)/Fe(20 nm) film stack. Bottom left panel: resistance versus field curve, measured at 10 mV positive bias, branch from the positive to negative field (-●-) and branch from negative to positive field (-○-). Right panel: sketch indicating the magnetization configurations in the stack within different field windows from (1) to (7).

anisotropy. The different magnetic configurations are detailed in the right panel sketch. At saturation (state 1) all the Fe layers have their magnetization parallel to the field. Reducing the field, the AF coupling tends to stabilize the AF configuration within the AAF. Therefore, during its reversal (in state 2) the magnetization of the thinner Fe_{II} layer of the AAF 'flips' to 90° with respect to the field, being 'temporarily' trapped by the second, easy-axis-related, anisotropy quantum well of Fe. In state 3 the AAF is stabilized in the AF configuration, with the net magnetic moment aligned along the positive field. Changing the sign of the field, the bottom Fe–I layer reverses its magnetization (state 4) following the field direction, then the net moment of the AAF switches along the field direction in state 5. Further increasing the field, the AAF will saturate (state 7) passing again through the intermediate 90° configuration of Fe_{II} (state 6).

The corresponding TMR curve is presented in the bottom panel of figure 16. The curve is measured at a bias voltage of 10 mV on a square 10 μm lateral size MTJ with an areal resistance of 2.9×10^5 Ω μm^2. The field variation of the resistance validates the magnetic configurations described above in the macroscopic magnetization curve. Indeed, we observe the smallest resistance in (1), corresponding to the parallel configuration of magnetization, and a maximum of the tunnel resistance in (3), corresponding to the anti-parallel configuration. In the intermediate states (2) and (6) one finds an intermediate resistance stage related to the 90° configuration of Fe_{II}. In these steps one can also expect the subsistence of some magnetic inhomogeneities within the AAF layers created during reversal of the magnetization [44]. Additional investigations by magnetic force microscopy under applied field are in progress.

Bearing in mind the thickness of the two tunnel barriers of the double junction, one can imagine that the voltage drop will mainly take place across the bottom thick MgO_I barrier. Therefore, here the measured resistance reflects the TMR effect of this barrier. However, coherent tunnelling events within the whole stack should be considered if the thickness of the intermediate Fe_{II} layer is decreased below 10 nm (the reported coherence length for the

majority spin in single-crystal Fe is above 10 nm, being 10 times smaller for the minority spin). All these aspects are currently under investigation.

6. Conclusion

In this paper we confronted the theoretical predictions concerning the spin transport and the wavefunction filtering in terms of symmetry in single-crystal MTJs. The experimental work was performed on Fe/MgO/Fe type MTJ systems manufactured by molecular beam epitaxy.

In the equilibrium regime, when the junctions are not biased, spin polarized tunnel transport leads to antiferromagnetic exchange interactions. An interesting class of artificial antiferromagnetic systems has been elaborated and studied.

The out-of-equilibrium regime is investigated for large MgO barrier thickness, where the filtering effect in k favours the tunnel propagation of electrons with k close to $k_\parallel = 0$. Moreover, the symmetry dependent attenuation rate in the barrier reduces the number of symmetry related conduction channels. This simplifies the analysis of the multi-channel transport mechanisms. We illustrated that the chemical and electronic structure of the interface has a major role in the tunnelling and filtering effects. Lastly, we presented an interesting class of double barrier system combining a classic Fe/MgO MTJ and an artificial antiferromagnetic subsystem in which the magnetic properties are controlled by coupling by spin polarized tunnelling.

## Appendix. Analytical model for an artificial anti-ferromagnetic system

We consider that the magnetic layers present a four-fold anisotropy, K_1, K_2 being the anisotropies of layers 1 and 2 of thickness t_1 and t_2 and magnetizations M_1 and M_2. The bilinear coupling is J, $\theta_{1,2}$ represent the angles between the magnetizations $M_{1,2}$ and the field H, φ the angle between one of the easy axes (A) and the field H, the other easy axis (B) is perpendicular to (A) (four-fold anisotropy). Figure A.1 presents schematically the macrospin Stoner–Wolfhart model used in our modelling.

Within this model the total energy of the AAF is given by

$$E_{\text{total}} = -H \times (M_1 t_1 \cos\theta_1 + M_2 t_2 \cos\theta_2) - J\cos(\theta_1 - \theta_2) + \frac{K_1 t_1}{4}\sin^2 2(\theta_1 - \varphi)$$

$$+ \frac{K_2 t_2}{4}\sin^2 2(\theta_2 - \varphi).$$
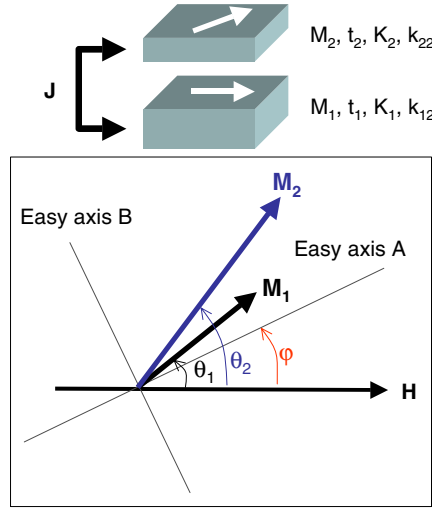
Figure A.1. Schematic representation of the macrospin Stoner–Wolfhart model. The four-fold easy axes are denoted by *A* and *B*. The field *H* is applied at an angle φ with respect to the *A* easy axis. In an arbitrary configuration, the magnetization M_i of layer *i* of thickness t_i, anisotropy K_i, k_{i2} makes an angle θ_i with respect to the field. The magnetic coupling between the two layers is denoted by *J*.

The first term represents the Zeeman energy, the second the bilinear coupling energy and the last two terms the anisotropy energy.

The minimization of the total energy $\frac{\partial E}{\partial \theta_1} = 0$ and $\frac{\partial E}{\partial \theta_2} = 0$ leads to the following equations:

$$\sin(\theta_2 - \theta_1) = \frac{1}{J} [MHt_1 \sin\theta_1 + K_1 t_1 \sin 2(\theta_1 - \varphi) \cos 2(\theta_1 - \varphi)]$$

$$-\sin(\theta_2 - \theta_1) = \frac{1}{J} [MHt_2 \sin\theta_2 + K_2 t_2 \sin 2(\theta_2 - \varphi) \cos 2(\theta_2 - \varphi)].$$

These equations can be solved in several specific situations.

A.1. Easy axis ($\varphi = 0$)

In order to compute the saturation field H_s and the plateau field H_P one can rewrite the general equations for $\varphi = 0$ in the form

$$\frac{\sin\theta_1}{\sin(\theta_2 - \theta_1)} = \frac{J}{t_1} \frac{1}{[MH + 2K_1 \cos\theta_1 \cos 2\theta_1]}$$

$$-\frac{\sin\theta_2}{\sin(\theta_2 - \theta_1)} = \frac{J}{t_2} \frac{1}{[MH + 2K_2 \cos\theta_2 \cos 2\theta_2]}.$$

By summing the two equations we obtain

$$\frac{\sin\theta_1 - \sin\theta_2}{\sin(\theta_2 - \theta_1)} = \frac{J}{t_1} \frac{1}{[MH + 2K_1 \cos\theta_1 \cos 2\theta_1]} + \frac{J}{t_2} \frac{1}{[MH + 2K_2 \cos\theta_2 \cos 2\theta_2]}.$$

The saturation field for the easy axis denoted by H_S^F corresponds to the saturation of both magnetic layers, i.e. $\theta_1 \to 0^-$ and $\theta_2 \to 0^+$. Moreover, we have

$$\frac{\sin\theta_1 - \sin\theta_2}{\sin(\theta_2 - \theta_1)} = \frac{2\cos(\frac{\theta_1 + \theta_2}{2}) \sin(\frac{\theta_1 - \theta_2}{2})}{2\cos(\frac{\theta_2 - \theta_1}{2}) \sin(\frac{\theta_2 - \theta_1}{2})} = -\frac{\cos(\frac{\theta_1 + \theta_2}{2})}{\cos(\frac{\theta_2 - \theta_1}{2})}$$

29

the limit $\theta_1 \to 0^-$ and $\theta_2 \to 0^+$ gives

$$-1 = \frac{J}{t_1} \frac{1}{\left[M H_{\text{S}}^{\text{F}} + 2K_1 \right]} + \frac{J}{t_2} \frac{1}{\left[M H_{\text{S}}^{\text{F}} + 2K_2 \right]}$$

which leads to a second-order equation with respect to H_{S}^{F} whose resolution gives

$$H_{\text{S}}^{\text{F}} + \frac{K_1 + K_2}{M} = -\frac{J}{2M} \left(\frac{1}{t_1} + \frac{1}{t_2} \right)$$

$$\times \left[1 \pm \sqrt{1 + \frac{4t_1 t_2 (t_1 - t_2)}{(t_1 + t_2)^2} \frac{(K_2 - K_1)}{J} + \frac{4t_1^2 t_2^2}{(t_1 + t_2)^2} \frac{(K_2 - K_1)^2}{J^2}} \right].$$

In order to determine the plateau field we now use the equations

$$\frac{\sin \theta_1 + \sin \theta_2}{\sin(\theta_2 - \theta_1)} = \frac{J}{t_1} \frac{1}{\left[MH + 2K_1 \cos \theta_1 \cos 2\theta_1 \right]} - \frac{J}{t_2} \frac{1}{\left[MH + 2K_2 \cos \theta_2 \cos 2\theta_2 \right]}$$

combined with

$$\frac{\sin \theta_1 + \sin \theta_2}{\sin(\theta_2 - \theta_1)} = \frac{2 \cos(\frac{\theta_1 - \theta_2}{2}) \sin(\frac{\theta_1 + \theta_2}{2})}{2 \cos(\frac{\theta_2 - \theta_1}{2}) \sin(\frac{\theta_2 - \theta_1}{2})} = -\frac{\sin(\frac{\theta_1 + \theta_2}{2})}{\sin(\frac{\theta_2 - \theta_1}{2})}.$$

The determination of the plateau field H_{P}^{F} implicates the limit situation: $\theta_1 \to 0^-$ and $\theta_2 \to \pi^-$ which leads to

$$1 = \frac{J}{t_1} \frac{1}{\left[M H_{\text{P}}^{\text{F}} + 2K_1 \right]} - \frac{J}{t_2} \frac{1}{\left[M H_{\text{P}}^{\text{F}} - 2K_2 \right]}$$

which corresponds again to a second-order equation in H_{P}^{F}. The solution of this equation gives the plateau field along the easy axis

$$H_{\text{P}}^{\text{F}} - \frac{K_2 - K_1}{M} = -\frac{J(t_1 - t_2)}{2t_1 t_2 M}$$

$$\times \left[1 \pm \sqrt{1 - \frac{4t_1 t_2 (t_1 + t_2)}{(t_1 - t_2)^2} \frac{(K_1 + K_2)}{J} + \frac{4t_1^2 t_2^2}{(t_1 - t_2)^2} \frac{(K_1 + K_2)^2}{J^2}} \right].$$

In these expressions the sign $\pm$ implies two possible solutions for the saturation and the plateau fields. The analysis of the solution in the limit case when $K_1 = K_2 = 0$ allows us to chose only the physically valid solutions

$$H_{\text{S}}^{\text{F}} + \frac{K_1 + K_2}{M} = -\frac{J}{2M} \left(\frac{1}{t_1} + \frac{1}{t_2} \right)$$

$$\times \left[1 + \sqrt{1 + \frac{4t_1 t_2 (t_1 - t_2)}{(t_1 + t_2)^2} \frac{(K_2 - K_1)}{J} + \frac{4t_1^2 t_2^2}{(t_1 + t_2)^2} \frac{(K_2 - K_1)^2}{J^2}} \right]$$

and

$$H_{\text{P}}^{\text{F}} - \frac{K_2 - K_1}{M} = -\frac{J(t_1 - t_2)}{2t_1 t_2 M}$$

$$\times \left[1 + \sqrt{1 - \frac{4t_1 t_2 (t_1 + t_2)}{(t_1 - t_2)^2} \frac{(K_1 + K_2)}{J} + \frac{4t_1^2 t_2^2}{(t_1 - t_2)^2} \frac{(K_1 + K_2)^2}{J^2}} \right].$$

A.2. Hard axis ($\varphi = \pi/4$)

We can proceed in a similar way:

$$\frac{\sin\theta_1}{\sin(\theta_2 - \theta_1)} = \frac{J}{t_1} \frac{1}{[MH - 2K_1 \cos\theta_1 \cos 2\theta_1]}$$

$$-\frac{\sin\theta_2}{\sin(\theta_2 - \theta_1)} = \frac{J}{t_2} \frac{1}{[MH - 2K_2 \cos\theta_2 \cos 2\theta_2]}.$$

The limit $\theta_1 \to 0^-$ and $\theta_2 \to 0^+$ for the saturation field H_S^D and $\theta_1 \to 0^-$ and $\theta_2 \to \pi^-$ for the plateau field H_P^D along the hard axis gives

$$-1 = \frac{J}{t_1} \frac{1}{\left[MH_S^D - 2K_1\right]} + \frac{J}{t_2} \frac{1}{\left[MH_S^D - 2K_2\right]}$$

and

$$1 = \frac{J}{t_1} \frac{1}{\left[MH_P^D - 2K_1\right]} - \frac{J}{t_2} \frac{1}{\left[MH_P^D + 2K_2\right]}.$$

The resolution of these equations leads to the analytical solutions

$$H_S^D - \frac{K_1 + K_2}{M} = -\frac{J}{2M}\left(\frac{1}{t_1} + \frac{1}{t_2}\right)$$
$$\times \left[1 \pm \sqrt{1 + \frac{4t_1 t_2 (t_1 - t_2)}{(t_1 + t_2)^2} \frac{(K_2 - K_1)}{J} + \frac{4t_1^2 t_2^2}{(t_1 + t_2)^2} \frac{(K_2 - K_1)^2}{J^2}}\right]$$

and

$$H_P^D + \frac{K_2 - K_1}{M} = -\frac{J(t_1 - t_2)}{2t_1 t_2 M}$$
$$\times \left[1 \pm \sqrt{1 + \frac{4t_1 t_2 (t_1 + t_2)}{(t_1 - t_2)^2} \frac{(K_1 + K_2)}{J} + \frac{4t_1^2 t_2^2}{(t_1 - t_2)^2} \frac{(K_1 + K_2)^2}{J^2}}\right].$$

The physically valid solutions are then

$$H_S^D - \frac{K_1 + K_2}{M} = -\frac{J}{2M}\left(\frac{1}{t_1} + \frac{1}{t_2}\right)$$
$$\times \left[1 + \sqrt{1 + \frac{4t_1 t_2 (t_1 - t_2)}{(t_1 + t_2)^2} \frac{(K_2 - K_1)}{J} + \frac{4t_1^2 t_2^2}{(t_1 + t_2)^2} \frac{(K_2 - K_1)^2}{J^2}}\right]$$

and

$$H_P^D + \frac{K_2 - K_1}{M} = -\frac{J(t_1 - t_2)}{2t_1 t_2 M}$$
$$\times \left[1 + \sqrt{1 + \frac{4t_1 t_2 (t_1 + t_2)}{(t_1 - t_2)^2} \frac{(K_1 + K_2)}{J} + \frac{4t_1^2 t_2^2}{(t_1 - t_2)^2} \frac{(K_1 + K_2)^2}{J^2}}\right].$$

31

A.3. Limit situations

We can consider first the case of isotropic magnetic layers ($K_1 = K_2 = 0$). This limit gives the following simplified expressions for the saturation and the plateau fields:

$$H_S = -\frac{J}{M}\left(\frac{1}{t_1} + \frac{1}{t_2}\right)$$

$$H_P = -\frac{J}{M}\frac{(t_1 - t_2)}{t_1 t_2}.$$

Note that in the isotropic limit all the directions are equivalent, which is also validated by the limit equal values of $H_S^E = H_S^D = H_S$ and $H_P^E = H_P^D = H_P$.

We can define the factor Q given by

$$\frac{H_S}{H_P} = \frac{t_1 + t_2}{t_1 - t_2} = Q.$$

One can demonstrate that the Q factor also represents the amplification factor for the coercive field of the AAF [43]. For an AAF in the AF plateau the net magnetic moment is reduced ($M_1 - M_2$), which reduces the sensitivity in external fields by the factor $t_1 - t_2$. Moreover within the monoblock strong AF coupling of the total friction of the magnetization with respect to external fields is increased by a factor proportional to $t_1 + t_2$. Then, roughly, the coercive field of an AAF is the coercive field of one of its single layers multiplied by the factor Q.

If $K_1 = K_2 = K$ then we obtain

$$H_S^F + \frac{2K}{M} = -\frac{J}{M}\left(\frac{1}{t_1} + \frac{1}{t_2}\right)$$

$$H_S^D - \frac{2K}{M} = -\frac{J}{M}\left(\frac{1}{t_1} + \frac{1}{t_2}\right)$$

$$H_P^F = -\frac{J(t_1 - t_2)}{2t_1 t_2 M}\left[1 \pm \sqrt{1 - \frac{8t_1 t_2(t_1 + t_2)}{(t_1 - t_2)^2}\frac{K}{J} + \frac{16t_1^2 t_2^2}{(t_1 - t_2)^2}\frac{K^2}{J^2}}\right]$$

and

$$H_P^D = -\frac{J(t_1 - t_2)}{2t_1 t_2 M}\left[1 \pm \sqrt{1 + \frac{8t_1 t_2(t_1 + t_2)}{(t_1 - t_2)^2}\frac{K}{J} + \frac{16t_1^2 t_2^2}{(t_1 - t_2)^2}\frac{K^2}{J^2}}\right].$$

If the AAF is compensated ($t_1 = t_2$) then

$$H_S^F + \frac{2K}{M} = -\frac{2J}{Mt}$$

$$H_S^D - \frac{2K}{M} = -\frac{2J}{Mt}.$$

A.4. Inequivalent anisotropy axes

In epitaxial systems the growth of samples in oblique geometry may give rise to inequivalent anisotropy values for the four-fold axes. In order to include this inequivalent anisotropy for

the four-fold axes one can simply add a second-order anisotropy for each easy axis (φ and $\varphi + \pi/2$). We denote these two-fold anisotropies by k_{12} and k_{22}. This will add some additional second-order anisotropy terms in the total energy:

$$E_{\text{totale}} = -H \times (M_1 t_1 \cos\theta_1 + M_2 t_2 \cos\theta_2) - J\cos(\theta_1 - \theta_2) + \frac{K_1 t_1}{4}\sin^2 2(\theta_1 - \varphi)$$

$$+ \frac{K_2 t_2}{4}\sin^2 2(\theta_2 - \varphi) + k_{12}t_1\sin^2(\theta_1 - \varphi) + k_{22}t_2\sin^2(\theta_2 - \varphi).$$

Along the easiest axis (A) which corresponds to $\varphi = 0$ the energy minimization leads to

$$\frac{\sin\theta_1}{\sin(\theta_2 - \theta_1)} = \frac{J}{t_1}\frac{1}{[MH + 2K_1\cos\theta_1\cos 2\theta_1 + 2k_{12}\cos\theta_1]}$$

$$-\frac{\sin\theta_2}{\sin(\theta_2 - \theta_1)} = \frac{J}{t_2}\frac{1}{[MH + 2K_2\cos\theta_2\cos 2\theta_2 + 2k_{22}\cos\theta_2]}$$

whereas along the other easy axis (B), which corresponds to $\varphi = \pi/2$, one obtains

$$\frac{\sin\theta_1}{\sin(\theta_2 - \theta_1)} = \frac{J}{t_1}\frac{1}{[MH + 2K_1\cos\theta_1\cos 2\theta_1 - 2k_{12}\cos\theta_1]}$$

$$-\frac{\sin\theta_2}{\sin(\theta_2 - \theta_1)} = \frac{J}{t_2}\frac{1}{[MH + 2K_2\cos\theta_2\cos 2\theta_2 - 2k_{22}\cos\theta_2]}.$$

Similar to the previous analysis, the limit situations leads to the following expressions: for the easiest axis (A)

$$H_{\text{S}}^A + \frac{K_1 + k_{12} + K_2 + k_{22}}{M} = -\frac{J}{2M}\left(\frac{1}{t_1} + \frac{1}{t_2}\right)$$

$$\times\left[1 + \sqrt{1 + \frac{4t_1 t_2(t_1 - t_2)}{(t_1 + t_2)^2}\frac{(K_2 + k_{22} - K_1 - k_{12})}{J} + \frac{4t_1^2 t_2^2}{(t_1 + t_2)^2}\frac{(K_2 + k_{22} - K_1 - k_{12})^2}{J^2}}\right]$$

and

$$H_{\text{P}}^A - \frac{K_2 + k_{22} - K_1 - k_{12}}{M} = -\frac{J(t_1 - t_2)}{2t_1 t_2 M}$$

$$\times\left[1 + \sqrt{1 - \frac{4t_1 t_2(t_1 + t_2)}{(t_1 - t_2)^2}\frac{(K_1 + k_{12} + K_2 + k_{22})}{J} + \frac{4t_1^2 t_2^2}{(t_1 - t_2)^2}\frac{(K_1 + k_{12} + K_2 + k_{22})^2}{J^2}}\right].$$

For the other easy axis (B)

$$H_{\text{S}}^B + \frac{K_1 - k_{12} + K_2 - k_{22}}{M} = -\frac{J}{2M}\left(\frac{1}{t_1} + \frac{1}{t_2}\right)$$

$$\times\left[1 + \sqrt{1 + \frac{4t_1 t_2(t_1 - t_2)}{(t_1 + t_2)^2}\frac{(K_2 - k_{22} - K_1 + k_{12})}{J} + \frac{4t_1^2 t_2^2}{(t_1 + t_2)^2}\frac{(K_2 - k_{22} - K_1 + k_{12})^2}{J^2}}\right]$$

and

$$H_{\text{P}}^B - \frac{K_2 - k_{22} - K_1 + k_{12}}{M} = -\frac{J(t_1 - t_2)}{2t_1 t_2 M}$$

$$\times\left[1 + \sqrt{1 - \frac{4t_1 t_2(t_1 + t_2)}{(t_1 - t_2)^2}\frac{(K_1 - k_{12} + K_2 - k_{22})}{J} + \frac{4t_1^2 t_2^2}{(t_1 - t_2)^2}\frac{(K_1 - k_{12} + K_2 - k_{22})^2}{J^2}}\right].$$

If we suppose now that $k_1 = K_2 = K$ and $k_{12} = k_{22} = k$ we obtain the following equations:

$$H_{\text{S}}^A + \frac{2(K + k)}{M} = -\frac{J}{M}\left(\frac{1}{t_1} + \frac{1}{t_2}\right)$$

33

$$H_S^B + \frac{2\,(K-k)}{M} = -\frac{J}{M}\left(\frac{1}{t_1} + \frac{1}{t_2}\right)$$

whose resolution gives

$$k = \frac{M}{4}\left(H_{S_1} - H_{S_2}\right).$$

This means that by measuring the saturation field along each of the two easy axes one can extract information about the second-order anisotropy.

The above analytical model has been used to extract exact analytical expressions for the critical fields (saturation and plateau). It may be useful to calculate the values of $\theta_1(H)$ and $\theta_2(H)$ for each value of the field H from positive saturation field to negative saturation field. This implicates the minimization of the total energy, point by point $\frac{\partial E(H)}{\partial \theta_1(H)} = 0$ and $\frac{\partial E(H)}{\partial \theta_2(H)} = 0$. This can be performed numerically (i.e. by steepest-descent, conjugated gradient or Metropolis/Monte Carlo algorithms).

References

[1] Moodera J S, Kinder L R, Wong T M and Meservey R 1995 *Phys. Rev. Lett.* **74** 3273
[2] Wolf S A 2000 *J. Supercond.* **13** 195
    Daughton J M 1997 *J. Appl. Phys.* **81** 3758
    Gallagher W J, Kaufman J H, Parkin S S P and Scheuerlin R E 1997 *US Patent Specification* 5 640 343
[3] Butler W H, Zhang X-G, Wang X, van Ek J and MacLaren J M 1997 *J. Appl. Phys.* **81** 5518
    Butler W H, Zhang X-G, Schulthess T C and MacLaren J M 2001 *Phys. Rev.* B **63** 054416
[4] MacLaren J M, Zhang X-G, Butler W H and Wang X 1999 *Phys. Rev.* B **59** 5470
[5] Mathon J and Umerski A 2001 *Phys. Rev.* B **63** 220403(R)
[6] Keavney D J, Fullerton E E and Bader S D 1996 *J. Appl. Phys.* **81** 795
[7] Klaua M, Ullmann D, Barthel J, Wulfhekel W, Kirschner J, Urban R, Monchesky T L, Enders A, Cochran J F and
    Heinrich B 2001 *Phys. Rev.* B **64** 134411
[8] Bowen M, Cros V, Petroff F, Fert A, Martinez Boubeta C, Costa-Kramer J L, Anguita J V, Cebollada A,
    Briones F, de Teresa J M, Morellon L, Ibarra M R, Guell F, Peiro F and Cornet A 2001 *Appl. Phys. Lett.*
    79 1655
[9] Faure-Vincent J, Tiusan C, Jouguelet E, Canet F, Sajieddine M, Bellouard C, Popova E, Hehn M, Montaigne F and
    Schuhl A 2003 *Appl. Phys. Lett.* **82** 4507
[10] Tiusan C, Sicot M, Faure-Vincent J, Hehn M, Bellouard C, Montaigne F, Andrieu S and Schuhl A 2006 *J. Phys.:
    Condens. Matter* **18** 941–56
[11] de Buttet C, Hehn M, Montaigne F, Tiusan C, Malinowski G, Schuhl A, Snoeck E and Zoll S 2006 *Phys. Rev.* B
    73 104439
[12] Tiusan C, Faure-Vincent J, Bellouard C, Hehn M, Jouguelet E and Schuhl A 2004 *Phys. Rev. Lett.* **93** 106602
[13] Tiusan C, Sicot M, Hehn M, Belouard C, Andrieu S, Montaigne F and Schuhl A 2006 *Appl. Phys. Lett.* **88** 62512
[14] Yuasa S, Nagahama T, Fukushima A, Suzuki Y and Ando K 2004 *Nat. Mater.* **3** 868
[15] Yuasa S, Katayama T, Nagahama T, Fukushima A, Kubota H, Suzuki Y and Ando K 2005 *Appl. Phys. Lett.*
    87 222508
    Yuasa S, Fukushima A, Kubota H, Suzuki Y and Ando K 2006 *Appl. Phys. Lett.* **89** 042505
[16] Tusche C, Meyerheim H L, Jedrecy N, Renaud G, Ernst A, Henk J, Bruno P and Kirschner J 2005 *Phys. Rev.
    Lett.* **95** 176101
[17] Dimopoulos T, Gieres G, Wecker J, Wiese N, Luo Y and Samwer K 2005 *J. Appl. Phys.* **98** 073705
[18] Parkin S S P, Kaiser C, Panchula A, Rice P M, Hughes B, Samant M and Yang S-H 2004 *Nat. Mater.* **3** 862
[19] Yuasa S, Fukushima A, Nagahama T, Ando K and Suzuki Y 2004 *Japan. J. Appl. Phys.* **43** (4B)
    Djayaprawira D D, Tsunekawa K, Nagai M, Maehara H, Yamagata S, Watanabe N, Yuasa S, Suzuki Y and
    Ando K 2005 *Appl. Phys. Lett.* **86** 092502
[20] Shen W, Mazumdar D, Zou X, Liu X, Schrag X B D and Xiao G 2006 *Appl. Phys. Lett.* **88** 182508
[21] Hayakawa J, Ikeda S, Matsukura F, Takahashi H and Ohno H 2005 *Japan. J. Appl. Phys.* **44** L587
[22] Tsunekawa K, Djayaprawira D D, Nagai M, Maehara H, Yamagata S, Watanabe N, Yuasa S, Suzuki Y and
    Ando K 2005 *Appl. Phys. Lett.* **87** 72503

[23] Kubota H, Fukushima A, Ootani Y, Yuasa S, Ando K, Maehara H, Tsunekawa K, Djayaprawira D, Watanabe N and Suzuki Y 2005 *IEEE Trans. Magn.* **41** 2633–5

[24] Ikeda S, Hayakawa J, Lee Y M, Tanikawa T, Matsukura F and Ohno H 2006 *J. Appl. Phys.* **99** 08A907

[25] Diao Z, Apalkov D, Pakala M, Ding Y, Panchula A and Huai Y 2005 *Appl. Phys. Lett.* **87** 232502

[26] Tulapurkar A A, Suzuki Y, Fukushima A, Kubota H, Maehara H, Tsunekawa K, Djayaprawira D D, Watanabe N and Yuasa S 2005 *Nature* **438** 339

[27] Nozaki T, Tezuka N and Inomata K 2006 *Phys. Rev. Lett.* **96** 27208

[28] Slonczewski J C 1989 *Phys. Rev.* B **39** 6995

[29] Tedrow P M and Meservey R 1994 *Phys. Rep.* **238** 174

[30] Julliere M 1975 *Phys. Lett.* **26** 192

[31] Zhang X-G and Butler W H 2003 *J. Phys.: Condens. Matter* **15** R1603

[32] Brinkman W F, Dynes R C and Rowell J M 1971 *J. Appl. Phys.* **41** 1915

[33] Bellini V 2000 *PhD Thesis* Rheinisch-Westfalischen Technische Hochschule Aachen, p 121
Dederichs P H *et al* 2002 *J. Magn. Magn. Mater.* **240** 108–13

[34] Velev J P, Belashchenko K D, Stewart D A, van Schilfgaarde M, Jaswal S S and Tsymbal E Y 2005 *Phys. Rev. Lett.* **95** 216601

[35] Bowen M, Barthelemy A, Bellini V, Bibes M, Seneor P, Jacquet E, Contour J-P and Dederichs P H 2006 *Phys. Rev.* B **73** 140408

[36] Stroscio J A, Pierce D T, Davies A, Celotta R J and Weinert M 1995 *Phys. Rev. Lett.* **75** 2960–3

[37] Wunnicke O, Papanikolaou N, Zeller R, Dederichs P H, Drchal V and Kudrnovsky J 2002 *Phys. Rev.* B **65** 064425

[38] Ding H F, Wulfhekel W, Henk J, Bruno P and Kirschner J 2003 *Phys. Rev. Lett.* **90** 116603

[39] Faure-Vincent J, Tiusan C, Bellouard C, Popova E, Hehn M, Montaigne F and Schuhl A 2002 *Phys. Rev. Lett.* **89** 107206

[40] Zhuravlev M Y, Tsymbal E Y and Vedyayev A V 2005 *Phys. Rev. Lett.* **94** 026806

[41] Bruno P 1995 *Phys. Rev.* B **52** 411

[42] Blum V, Schmidt A, Meier W, Hammer L and Heinz K 2003 *J. Phys.: Condens. Matter* **15** 3517

[43] van den Berg H A M, Clemens W, Gieres G, Rupp G, Vieth M, Wecker J and Zoll S 1997 *J. Magn. Magn. Mater.* **165** 524

[44] Tiusan C, Dimopoulos T, Ounadjela K, Hehn M, van den Berg H A M, Henry Y and Da Costa V 2000 *Phys. Rev.* B **61** 580

[45] Tiusan C, Hehn M and Ounadjela K 2002 *Eur. Phys. J.* B **26** 431

[46] Belashchenko K D, Velev J and Tsymbal E Y 2005 *Phys. Rev.* B **72** R140404

[47] Popova E, Faure-Vincent J, Tiusan C, Bellouard C, Fischer H, Hehn M, Montaigne F, Alnot M, Andrieu S, Schuhl A, Snoeck E and da Costa V 2002 *Appl. Phys. Lett.* **81** 1035

[48] Zhang X-G and Butler W 2003 *J. Phys.: Condens. Matter* **15** R1603

[49] Stoeffler D 2004 private communication

[50] Blaha P, Schwarz K, Madsen G K H, Kvasnicka D and Luitz J 2001 *WIEN2k, An Augmented Plane Wave + Local Orbitals Program for Calculating Crystal Properties (Techn. Univ. Wien, Austria)* ed K Schwartz (ISBN 3-9501031-1-2)

[51] Zhang X-G, Butler W H and Bandyopadhyay A 2003 *Phys. Rev.* B **68** 092402

[52] Jansen R and Moodera J S 2000 *Phys. Rev.* B **61** 9047

[53] de Teresa J M, Barthelemy A, Fert A, Contour J P, Montaigne F and Seneor P 1999 *Science* **286** 507

[54] Zhang S, Levy P M, Marley A C and Parkin S S P 1997 *Phys. Rev. Lett.* **79** 3744
Moodera J S, Nowak J and van de Veerdonk R J M 1998 *Phys. Rev. Lett.* **80** 2941

[55] Pajda M, Kudrnovsky J, Turek I, Drchal V and Bruno P 2001 *Phys. Rev.* B **64** 174402

[56] Parlinski K, Lazewski J and Kawazoe Y 2000 *J. Phys. Chem. Solids* **61** 87

[57] Bardou F 1997 *Europhys. Lett.* **39** 239
Da Costa V, Romeo M and Bardou F 2003 *J. Magn. Magn. Mater.* **258/259** 90

[58] Da Costa V, Tiusan C, Dimopoulos T and Ounadjela K 2000 *Phys. Rev. Lett.* **85** 876

[59] Przybylski M, Grabowski J, Wulfhekel W, Rams M, Tomala K and Kirschner J 2004 *J. Appl. Phys.* **95** 597